Self-assembly of CIP4 drives actin-mediated asymmetric pit-closing in clathrin-mediated endocytosis

Yiming Yu and Shige H. Yoshimura*

Graduate School of Biostudies, Kyoto University, Kyoto 606-8501, Japan

*Corresponding author

Shige H. Yoshimura

Graduate School of Biostudies, Kyoto University, Kyoto 606-8501, Japan

E-mail: yoshimura@lif.kyoto-u.ac.jp

Tel & Fax: +81-75-753-7906

ORCID: 0000-0001-6033-1301

Abstract

Clathrin-mediated endocytosis is pivotal to signal transduction pathways between the extracellular environment and the intracellular space. Evidence from live-cell imaging and super-resolution microscopy of mammalian cells suggests an asymmetric distribution of actin fibres near the clathrin-coated pit, which induces asymmetric pit-closing rather than radial constriction. However, detailed molecular mechanisms of this 'asymmetricity' remain elusive. Herein, we used high-speed atomic force microscopy to demonstrate that CIP4, a multi-domain protein with a classic F-BAR domain and intrinsically disordered regions, is necessary for asymmetric pit-closing. Strong self-assembly of CIP4 via intrinsically disordered regions, together with stereospecific interactions with the curved membrane and actin-regulating proteins, generates a small actin-rich environment near the pit, which deforms the membrane and closes the pit. Our results provide mechanistic insights into how disordered and structured domain collaboration promotes spatio-temporal actin polymerisation near the plasma membrane.

Introduction

Clathrin-mediated endocytosis (CME) is necessary for several cellular processes, including low-density lipoprotein uptake, epidermal growth factor receptor signalling transduction, synaptic vesicle formation, and cell migration[1-3]. Clathrin-dependent endocytic machinery is highly disciplined in recruiting and disassembling over 60 endocytic proteins in an ordered sequence[4]. Clathrin-coated pit (CCP) initiation requires the assembly of several adaptors and scaffold proteins, including the Fes/Cip4 homology Bin/amphiphysin/Rvs (F-BAR) domain-only protein, Eps15, AP2 complex, and intersectin[5-10]. Polymerised clathrin forms a hexagonal lattice that curves the plasma membrane and gradually drives CCP invagination[11]. In the late CME stage, highly invaginated CCPs are detached from the membrane via dynamin-mediated constriction and scission and then transported to the cytosol for further processing[12,13].

The pit-closing step of CME has recently attracted much research attention owing to the series of processes involved, including membrane deformation, fusion, and scission. In addition to a canonical dynamin-dependent constriction mechanism, actin is crucial to the endocytic progression in yeast and mammals[14]. In yeast cells, actin assembles symmetrically at the base of the CCP in a radial distribution and constricts the membrane tubule[15]. In mammalian cells, actin functions as a force generator that counteracts

membrane tension, elongates the membrane tubules, and assists in forming deeply-invaginated vesicles[16-18]. Furthermore, actin coordinates other endocytic proteins, such as dynamin and BAR domain proteins, to promote the constriction and scission of the membrane tubules before vesicle translocation[19-21].

Asymmetric distribution revealed via total internal reflection fluorescence microscopy is an interesting characteristic of the actin cytoskeleton around CCP[22]. Recent progress in super-resolution techniques further revealed that many endocytic proteins possess unique localisation around the clathrin lattice[23] and that actin and some associated proteins, including the neural Wiskott–Aldrich syndrome protein (N-WASP) and actin-related proteins-2/3 (Arp2/3) complex, asymmetrically assemble near the CCP[24]. Correspondingly, live-cell imaging with ion conductance microscopy revealed a membrane bulge that asymmetrically formed around the CCP and gradually covered that area[25].

Correlative imaging of high-speed atomic force microscopy (HS-AFM) and confocal laser-scanning microscopy (CLSM) is powerful for investigating the morphological changes of the plasma membrane during endocytosis[26]. Our previous study using this technique has revealed a good correlation between the progress of membrane invagination and the clathrin signal accumulation supporting the hotly debated 'constant curvature model[27,28]'. Moreover, we observed an asymmetric closing process dependent on Arp2/3-mediated actin polymerisation[27]. A lateral constriction is energetically more favourable for membrane fusion than a radial constriction[29]. Therefore, the actin-dependent asymmetric closing mechanism seems crucial in CME; however, the detailed molecular mechanism generating the asymmetric assembly of actin machinery remains elusive.

Herein, we studied the molecular mechanism underlying asymmetric actin assembly and the consequent generation of the membrane bulge near the CCP. We used live-cell HS-AFM and fluorescence-based imaging to examine the involvement of F-BAR domain-containing proteins (CIP4, FBP17, and Syndapin 2), which carry structured domains to interact with actin regulatory proteins and long, disordered domains in CME. Our results provide mechanistic insights into how a multi-domain protein can spatio-temporally recruit and orchestrate the actin machinery near the CCP via phase separation of disordered domains and stereospecific interactions between structured domains.

Results

69 **Asymmetric CCP closing**

70 Using HS-AFM, CME was described as a group of near-circular invaginations with diameters of 150–400 nm
71 and lifetimes of 40 to ~300 s[27]. This prior observation revealed various dynamic plasma membrane processes
72 during the CME. Three different closing patterns, namely, 'asymmetric', 'symmetric', and 'undetermined',
73 were identified (Fig. 1a, Extended Data Fig. 1a–1c). The asymmetric pattern is the dominant closing pattern
74 that corresponds to ~71% of total closing events (Fig. 1b), in which a membrane bulge emanates from one
75 side (or a limited area) of the CCP and covers the pit at the end (Fig. 1a, Extended Data Fig. 1a,
76 Supplementary Video 1). The diameter of the pit plummeted within 10–20 s before complete closing (Figs. 1a,
77 1c, Extended Data Fig. 1a). In the symmetric pattern (~18% of total events, Fig. 1b), the pit slowly shrank
78 isotropically and completely closed with a weak membrane bulge (Figs. 1a, 1c, Extended Data Fig. 1b,
79 Supplementary Video 2). A small portion of the pits (~10% of the total events, Fig. 1b) closed within 10–20 s
80 but without detectable bulges (Figs. 1a, 1c, Extended Data Fig. 1c, Supplementary Video 3). Moreover,
81 scanning with a higher time resolution (0.5 frames/s) did not reveal a membrane bulge around these pits
82 (Extended Data Fig. 1d); therefore, they were classified as 'undetermined'.

83 The asymmetric bulge grew faster (increase in the membrane height per unit time), higher (the
84 maximum height of the bulge), and continued for a longer period (duration of the bulge) than did the
85 symmetric bulge (Fig. 1d). However, CCPs with the asymmetric or symmetric closing patterns had a similar
86 total lifetime (Fig. 1d). The closing rate (reduction in the diameter per unit time) also differed: the asymmetric
87 pattern (8.3 ± 3.9 nm/s) was faster than the symmetric one (3.9 ± 1.8 nm/s) (Fig. 1d), suggesting that the pit-
88 closure is accelerated more by the asymmetric bulge than the symmetric bulge. Treatment with CK666, an
89 Arp2/3 complex inhibitor[30], and knockdown (KD) of N-WASP (Extended Data Fig. 1e), an upstream activator
90 of Arp2/3[31], promoted the frequency of newly formed CCPs while reducing the frequency of asymmetric and
91 symmetric bulges to ~17% and 0%, respectively (Fig. 1b, Extended Data Figs. 1f, 1g). This result
92 demonstrates that N-WASP- and Arp2/3-dependent actin polymerisation is required for bulge formation.

93

94 **CIP4 is necessary for asymmetric bulge formation**

95 We further identified the proteins that potentially mediate the asymmetric closing process. F-BAR domain-
96 containing proteins were ideal candidates to coordinate actin reorganisation with membrane deformation

97 during CME owing to their membrane deformation and actin-associated properties[32,33]. CIP4, Syndapin 2
98 (Synd2, also called Pacsin2), and FBP17 are classic F-BAR domain proteins localised at CCPs[22], and Cos7
99 cells express all these proteins (Extended Data Figs. 2a, 2b). The time-lapse fluorescence observations of
100 Cos7 cells expressing mCherry-fused CIP4, Synd2, or FBP17 with an enhanced green fluorescent protein
101 (EGFP)-fused clathrin light chain B (CLTB) revealed different timings and kinetics of their assembly at the
102 CCP (Fig. 2a, Extended Data Fig. 3a–3c). When the disappearance of the clathrin signal was set as time 0,
103 CIP4, Synd2, and FBP17 appeared at the CCP at -26.0 ± 7.4, -16.0 ± 5.5, and -10.5 ± 4.0 s and disassembled
104 at -5.0 ± 2.3, -7.8 ± 4.4, and -2.0 ± 6.0 s, respectively (Fig. 2b). CIP4 KD with two siRNA species (one for the
105 coding region, siCIP4_coding; one for the 3′ untranslated region, siCIP4_3′UTR) in Cos7 cells reduced the
106 frequency of the asymmetric bulges (from ~74% to <30%) and increased the undetermined pattern (~70%)
107 (Fig. 2c, Extended Data Fig. 2c–2e). Moreover, overexpression of EGFP-fused CIP4 in CIP4-KD
108 (siCIP4_3′UTR) cells rescued the asymmetric bulge (Fig. 2c, Extended Data Fig. 2d). By contrast, Synd2 or
109 FBP17 KD did not markedly affect any closing patterns (Fig. 2c, Extended Data Figs. 2c, 2d). Nevertheless,
110 the overall frequency of CME was unaffected (Extended Data Fig. 2f). These results demonstrate that CIP4,
111 but not FBP17 or Synd2, is necessary for the asymmetric bulge.
112 Correlative imaging of HS-AFM and CLSM revealed a clear correlation between the assembly of
113 CIP4 and the bulge formation. When the disappearance of the clathrin signal was set as time 0, CIP4 was
114 observed at -33.9 ± 6.50 s under CLSM, and the membrane bulge formed at -30.0 ± 8.16 s under the HS-AFM
115 (Fig. 2d, Extended Data Fig. 2g), indicating a strong association between CIP4 and bulge formation.
116 The relative position of CIP4 and the clathrin signal was determined using time-lapse super-
117 resolution structural illumination microscopy (SIM) to confirm the asymmetric localisation of CIP4. The CIP4
118 signal started to appear at the determined position offset from clathrin, with a centre-to-centre distance within
119 the first 5 s of 126.8 ± 66.6 nm (N = 160) (Figs. 2e, 2f, Extended Data Fig. 2h). As the CIP4 signal increased,
120 the centre-to-centre distance fluctuated with a decreasing tendency until both signals disappeared (Fig. 2e,
121 Extended Data Fig. 2h). Thus, we concluded that CIP4 was asymmetrically assembled at the CME site.
122
123 **Flanking disordered region is vital for CIP4 assembly in CCP**

124 The CIP4 domain required for self-assembly around CCP was subsequently determined. CIP4 and FBP17
125 belong to the same subfamily of F-BAR proteins and have conserved F-BAR and SH3 domains at the amino-
126 and carboxyl-termini, respectively (Extended Data Figs. 3d, 3e). The middle region between these conserved
127 domains is less conserved and mostly disordered without any known binding motifs for other endocytic
128 proteins (Fig. 3a, Extended Data Figs. 3d, 3e). In CIP4 and FBP17, but not Synd2, the middle-disordered
129 region is intervened by a conserved G protein-binding homology region 1 (HR1); therefore, it is named the
130 flanking disordered region (FDR; Fig. 3a, Extended Data Fig. 3d).

131 The CIP4 assembly at the CCP was unaffected by SH3 domain deletion (CIP4(ΔSH3); Fig. 3a–3c,
132 Extended Data Fig. 4a). BAR domain and the FDR were insufficient for CIP4 assembly (Fig. 3b), indicating
133 that the F-BAR domain and FDR are necessary for CIP4 to assemble at the CCP. Notably, the assembly of
134 chimeric molecules carrying the Synd2-BAR and CIP4-FDR (SCC and SC chimaeras in Fig. 3a) to the CCP
135 starts at a time point similar to that of full-length CIP4 (Figs. 3b, 3c, Extended Data Fig. 4a). By contrast, the
136 CS mutant, which carries the CIP4-BAR and Synd2-IDR (Fig. 3a), did not assemble at the CCP (Fig. 3b).
137 Therefore, these results demonstrate that the FDR of CIP4 is a major determinant of the self-assembly at the
138 CCP. However, the BAR domain is also necessary.

139

140 **SH3 domain is required for membrane bulge formation**

141 In contrast to the assembly at the CCP, the SH3 domain was required to form the membrane bulge. The SC
142 chimaera expression, which could assemble at the CCP (Fig. 3b), failed to rescue the CIP4-KD phenotype; the
143 frequency of the asymmetric membrane bulge was not recovered by the SC mutant expression (Fig. 3d). By
144 contrast, the SCC chimaera, which also carries the SH3 domain of CIP4, could rescue the KD phenotype (Fig.
145 3d), indicating that the SH3 domain was necessary for forming the membrane bulge after the assembly at the
146 CCP.

147 CIP4 binds and activates N-WASP via the SH3 domain[34]. The activated N-WASP interacts with
148 Cdc42 through its GTPase binding domain (GBD) (Extended Data Figs. 4b, 4c) and recruits the Arp2/3
149 complex to promote actin polymerisation[35]. In our experimental system, the assembly of N-WASP at the CCP
150 was also observed; it appeared at the CCP immediately after CIP4 (Extended Data Figs. 4d, 4e). Therefore, we
151 examined whether the interaction between CIP4 and N-WASP is necessary for the asymmetric bulge. A point

152 mutation in the SH3 domain of Toca1 (W518K) inhibited the interaction with N-WASP[36]. Mutating the
153 corresponding residue in the CIP4-SH3 domain (W524K) also reduced the interaction with N-WASP (Fig. 3e,
154 Extended Data Fig. 4f). In agreement with this finding, the SCC chimaera carrying the W524K mutation
155 failed to rescue the CIP4-KD phenotype (Fig. 3d), indicating that the interaction with CIP4-SH3 and N-WASP
156 is necessary for forming the asymmetric bulge.
157

158 **Cdc42 recruits CIP4 to the CCP site**

159 Next, we examined FDR's involvement in the asymmetric assembly of CIP4 at the CCP. We first focused on
160 the interaction with Cdc42[36]. A pull-down assay demonstrated that the CIP4-FDR had a higher affinity to the
161 active (GTPγS-loaded) form of Cdc42 than to the FBP17-FDR and the IDR of Synd2 (Fig. 4a, Extended Data
162 Fig. 5a). Substitutions of three amino acids within HR1 (MGD to IST, Extended Data Fig. 5b), which abolish
163 the interaction with Cdc42 in Toca1-HR1[35], also attenuated the interaction with Cdc42 (Fig. 4a, Extended
164 Data Fig. 5a). The assembly of full-length CIP4 carrying the MGD-IST mutation at the CCP started at -12.5 ±
165 5.2 s (Figs. 4b, 4c, Extended Data Fig. 5c), which was delayed compared to that of the wild-type (WT),
166 indicating that the activated Cdc42 is required for CIP4 assembly at the CCP.

167 The interaction with active Cdc42 was important for CIP4 assembly at the CCP and asymmetric
168 bulge formation. The overexpression of a dominant-negative form of Cdc42(T17N), but not the WT, severely
169 impaired the asymmetric bulge (to ~25%) compared to that of the non-transfected cells (Fig. 4d). In addition,
170 the SCC chimaera carrying the MGD-IST mutation failed to rescue the CIP4-KD phenotype (Fig. 4d). These
171 results indicated that activated Cdc42 recruits CIP4 to the CCP site, which further induces asymmetric bulge
172 formation.
173

174 **FDR self-assembly generates 'asymmetric' CIP4 distribution**

175 The interaction between Cdc42 and CIP4 is crucial in CIP4 assembly at the CCP; however, it does not explain
176 how 'asymmetricity' is produced. A possible mechanism could be the cooperativity of the assembly. The
177 structural prediction based on the amino acid sequence suggested that the HR1 of CIP4 forms a helical coil
178 composed of two antiparallel α-helices (Extended Data Fig. 6a). To examine the secondary structure of CIP4-
179 HR1, we measured the circular dichroism spectrum of recombinant HR1, which fitted well with that of the

180 reference curve of α-helix (Extended Data Fig. 6b), demonstrating a strong propensity of α-helix in HR1.
181 Therefore, we speculated that it forms a multimer and the association proceeds cooperatively. To test this
182 hypothesis, purified HR1 was subjected to gel-filtration chromatography to estimate the molecular size. We
183 observed that HR1 existed mainly as a dimer, and any multimers could not be detected under a physiological
184 condition (Extended Data Figs. 6c, 6d). A similar result was obtained by treating purified HR1 with
185 bis(sulfosuccinimidyl)suberate (BS^3) crosslinkers and analysing using SDS-PAGE. Adding crosslinkers
186 induced an extra band corresponding to the HR1 dimer, but not higher-order multimers (Extended Data Fig.
187 6e). Thus, these results demonstrate that HR1 multimerisation is not the major driving force of asymmetricity.
188 Another possibility could be the self-assembly and phase transition of FDR via electrostatic
189 interaction between IDRs. The HR1 domain of CIP4 and FBP17 is flanked by positively and negatively
190 charged IDRs at the amino and carboxyl sides, respectively (Fig. 5a, Extended Data Fig. 6f). By contrast, the
191 charge segregation of Synd2 IDR is not so prominent (Extended Data Fig. 6f). It has been well-established
192 that a polymer with segregated charges (i.e., block polyampholyte) exhibits stronger liquid–liquid phase
193 separation (LLPS) than the chain with the same number of charges randomly distributed (i.e., random
194 polyampholyte)[37,38], and the pattern of charge blocks is an important determinant of LLPS properties[39]. These
195 properties strongly suggest that the FDR self-assembles to undergo LLPS via charge-block interaction among
196 IDRs (Fig. 5a). To test this possibility, the purified recombinant protein was subjected to an *in vitro* droplet
197 assay in the presence of polyethene glycol as a crowder. CIP4-FDR formed protein droplets, unlike the IDR of
198 Synd2 (Fig. 5b). Quantification of protein droplets based on the turbidity revealed that the saturation
199 concentration of CIP4-FDR was similar to that of the FBP17-FDR but remarkably lower than that of the
200 Synd2-IDR (Figs. 5b, 5c), indicating that CIP4-FDR and FBP17-FDR has a stronger propensity for LLPS than
201 Synd2-IDR. Fluorescence recovery after photobleaching (FRAP) analysis revealed that the protein droplet
202 was in a liquid-like state (Fig. 5d). Deletion of either IDR (ΔIDR1 or ΔIDR2) from CIP4-FDR severely
203 attenuated the LLPS (Figs. 5c, 5e), demonstrating that the interaction between charge blocks is essential in the
204 LLPS of FDR.
205 Deleting one of the IDRs of CIP4-FDR did not completely abolish LLPS (Fig. 5e). Therefore, we
206 speculated that HR1 also contributes to LLPS. HR1 deletion from FDR (ΔHR1) partly, but significantly,
207 reduced the LLPS propensity (Figs. 5c, 5e). To substantiate this idea, intensive mutations were introduced into

208 HR1 to reduce dimer formation. We observed that substitutions of four hydrophobic residues (L347, L401,
209 Y408, and W411 labelled in Extended Data Fig. 6a) by serine (4S) disrupted the HR1-dimer without affecting
210 the interaction with Cdc42 (Fig. 4a, Extended Data Figs. 5a, 6c). As expected, the LLPS propensity of the
211 CIP4-FDR(4S) mutant was lower than that of the WT (Figs. 5c, 5e), indicating that HR1 dimerisation
212 promotes the FDR-dependent assembly of CIP4. To test whether FDR-driven LLPS is essential in CIP4
213 assembly at the CCP, we analysed the assembly rate of CIP4 through live-cell fluorescence imaging. SH3
214 deletion (CIP4(ΔSH3)) did not affect the assembly rate of CIP4 at CCP (Fig. 5f). Interestingly, further
215 deletion of IDR2(ΔIDR2/SH3), which reduces the LLPS propensity of CIP4-FDR (Figs. 5c, 5e), reduced the
216 assembly rate by ~70% (Fig. 5f, Extended Data Fig. 6g), implicating the role of phase separation in driving
217 CIP4 assembly at CCP. Similarly, the 4S mutation in the full-length CIP4 almost completely abolished the
218 assembly (Extended Data Fig. 6h), which was more severe than the IDR2 deletion. In agreement with this
219 finding, the SCC chimaera carrying the 4S mutation did not rescue the CIP4-KD (Extended Data Fig. 6i).
220 These observations indicated that the FDR-dependent LLPS is critical in CIP4 assembly at the CCP.
221 As we demonstrated, CIP4 assembly is closely associated with Cdc42 and N-WASP. We then
222 investigated whether these two regulators or effectors potentially affected the LLPS propensity of CIP4.
223 Cdc42 (WT and constitutively active form Q61L) did not undergo LLPS or enhance CIP4-FDR LLPS (Figs.
224 5c, 5g). These results demonstrate that the Cdc42-CIP4 interaction does not contribute to the LLPS of CIP4.
225 However, N-WASP exhibited strong LLPS (C_{sat}: ~10 μM) (Fig. 5c). Therefore, we examined whether N-
226 WASP and CIP4 co-exist in the same droplet or exclude each other. N-WASP and full-length CIP4 co-existed
227 in the same droplet (Fig. 5h). The same result was obtained with CIP4-FDR and N-WASP (Figs. 5g, 5h).
228 These results indicate that both proteins have a strong propensity for LLPS and tend to co-exist in the same
229 droplet.
230
231 **Actin amasses and polymerises in a liquid phase of CIP4-FDR**
232 We examined whether a liquid phase formed by CIP4-FDR could accelerate actin polymerisation. Alexa488-
233 labelled CIP4-FDR was mixed with polyethene glycol to induce LLPS, and then rhodamine-labelled G-actin
234 was added (Fig. 5i). The time-lapse observation under a fluorescence microscope revealed that actin rapidly

235 moved into the droplet (Fig. 5i). The concentration of actin was ~100 times higher in the droplet than in the
236 external medium, demonstrating that actin accumulated in the CIP4-FDR droplet.
237 We then tested whether actin polymerisation also occurs in the droplet. ATP and Mg^{2+} and a low
238 concentration of G-actin (45 μg/mL) were added to the droplet solution of CIP4-FDR to induce actin
239 polymerisation in the droplet (Figs. 5i, 5j). Under this condition, actin polymerisation rarely occurred in the
240 diluted phase, owing to the low actin concentration. However, fibrous actin was frequently observed in the
241 droplet (Fig. 5j). ATP depletion almost completely abolished it (Fig. 5j), demonstrating that actin
242 polymerisation occurs in the droplet. Thus, these results demonstrate that CIP4 self-assembles via FDR to
243 form a liquid-like phase and concentrates G-actin in the liquid phase to accelerate the polymerisation.
244
245 **Discussion**
246 Herein, we used various live-cell imaging techniques and biochemical approaches to demonstrate that the
247 BAR domain-containing protein CIP4 is critical in the actin-dependent asymmetric closing process of CME.
248 CIP4 interacts with curved membrane and actin-related proteins such as Cdc42 and N-WASP through its
249 distinct structured domains (i.e., BAR, HR1, and SH3). Our results demonstrated that the asymmetricity was
250 generated during the self-assembly of the disordered regions between those structured domains. This describes
251 an intriguing molecular mechanism of how a multi-domain protein, such as CIP4, spatio-temporally recruits
252 and orchestrates the actin machinery at a specific cell position. Strong self-assembly, phase separation of
253 IDRs, and stereospecific interactions between structured domains induce a local burst of branched actin fibres
254 nearby the CCP. It has been proposed that unstructured amino acid chains sense the curved lipid bilayer via
255 entropic or electrostatic mechanisms, determined by their length and net charge[40]. Recently, the IDRs of
256 membrane-bound, -anchored, and -embedded proteins, including AP180, Amphiphysin 1, FBP17, CALM, and
257 Epsin, are gaining more research attention for supporting or enhancing the membrane-bending or curvature-
258 sensing properties of the structured domains[41-45]. Therefore, our findings provide a novel perspective for
259 understanding the role of disordered proteins in CME progression.
260 Four members of F-BAR domain-containing proteins are CIP4, FBP17, Synd2, and Toca1. CIP4,
261 FBP-17, and Synd2 assemble at the CCP at different times during CME (Fig. 2b) and have different cellular
262 functions[32,46] despite their similar domain structures. This could partly be attributed to the slightly different

263 curvature of the three-dimensional structures of the BAR domains[46]. Herein, we demonstrated that the middle-
264 disordered regions between the BAR and SH3 domains had different self-assembly properties. The FDRs of
265 CIP4 and FBP17, but not the IDR of Synd2, had high LLPS propensity, and both disordered regions were
266 required for CIP4 phase separation (Figs. 5c, 5e). However, when either of the disordered regions was deleted
267 (ΔIDR1 or ΔIDR2), a certain level of LLPS propensity was preserved (Fig. 5e), suggesting that HR1
268 dimerisation may also promote the LLPS of FDR. These results clearly explain the functional diversity among
269 Synd2, CIP4, and FBP17 in CME and possibly other cellular processes in which they are involved.

270 In contrast to Synd2, the FBP17-FDR has a similar charge distribution pattern to that of CIP4
271 (Extended Data Fig. 6f) and exhibits a similar phase behaviour *in vitro* (Figs. 5b, 5c); however, they greatly
272 diverge regarding their functions and localisations. During CME, CIP4 assembles at the CCP before complete
273 pit-closure (Fig. 2d), which is remarkably earlier than that of FBP17 (Fig. 2b). Moreover, an *in vitro* pull-
274 down assay revealed that CIP4-FDR had a higher ability to bind to Cdc42 than does the FDR of FBP17 (Fig.
275 4a, Extended Data Fig. 5a); this implies that disordered regions have a role in Cdc42 interactions. In dendritic
276 neurons, FBP17 displayed an intracellular distribution different from that of CIP4 due to its poly PxxP region
277 within the first IDR[47]. These observations implicate the underestimated role of disordered regions in
278 regulating nearby stereospecific interactions.

279 CIP4 strongly self-assembled and underwent LLPS *in vitro* (Fig. 5b); nonetheless, the intracellular
280 concentration of endogenous CIP4, estimated from the total intracellular amount (~20 nM, Extended Data Fig.
281 6j), was far lower than the saturation concentration (~6 μM, Fig. 5c). These results suggested that in addition
282 to the charge block-driven LLPS of FDR, a certain mechanism which assembles CIP4 near the CCP for
283 'nucleation' is required to initiate LLPS. One important factor in this nucleation can be stereospecific
284 interactions involving the structured domains (F-BAR, HR1, and SH3).

285 In the absence of the CCP, CIP4 binds to active Cdc42 anchored to the plasma membrane via PIP_2
286 through the HR1 domain (Fig. 6a). CIP4 also binds to N-WASP via the SH3 domain, allowing the interaction
287 between N-WASP and Cdc42, and ternary complexes form among CIP4, N-WASP, and Cdc42 (Fig. 6b).
288 However, at this stage, the local concentration of CIP4 may not be sufficient to initiate LLPS (Fig. 6b). When
289 the ternary complex occasionally approaches the CCP, the BAR domain recognises the curvature of the pit
290 membrane and binds to it (Fig. 6c). The BAR domain multimerises on the membrane[48]; therefore, it

291 accelerates CIP4 assembly near the CCP. In good agreement with this finding, the LLPS propensity of full-
292 length CIP4 is higher than that of FDR (Fig. 5c), suggesting the involvement of the BAR domain in LLPS
293 progression.

294 Recent studies reported 'membrane-supported' LLPS at the plasma membrane and other intracellular
295 membrane organelles[49,50], where membrane-anchored or -inserted proteins assemble on the membrane and
296 'nucleate' for LLPS. This two-dimensional system can considerably accelerate LLPS compared to a dispersed
297 system and initiate LLPS regardless of the bulk (cytoplasmic) protein concentration being below the
298 threshold. We speculate that these stereospecific interactions (Cdc42-HR1, F-BAR-F-BAR, and F-BAR-
299 membrane) contribute to CIP4 nucleation near the CCP.

300 Once CIP4 nucleates near the CCP, it undergoes 'charge block-driven LLPS' via FDR and
301 condenses—a major driving force of 'asymmetric' CIP4 assembly (Fig. 6d). The F-BAR domain multimerises
302 and forms a helical structure around the tubulated membrane *in vitro*[48,51]. However, it is insufficient for the
303 assembly at the CCP, as we have demonstrated in this study (Fig. 3b). Furthermore, it does not provide a
304 structural basis for the 'asymmetric' distribution at the CCP. Instead, we speculate that LLPS is key to
305 forming the 'asymmetric' assembly of CIP4 because the emergence of a condensed phase proceeds in a non-
306 continuous manner when the local protein concentration is above the threshold. Therefore, F-BAR- and HR1-
307 driven nucleation and FDR-driven LLPS synergistically work for the fast assembly of CIP4 at the CCP. This
308 finding is consistent with the results of a previous study demonstrating that disordered domains enhance the
309 affinity of BAR domains to the curved membrane[41].

310 Our chimeric molecule between CIP4 and Synd2 demonstrated that the BAR domain was functionally
311 exchangeable (SCC chimaera, Fig. 3a–3c, Extended Data Fig. 4a), implying that the curvature-sensing by the
312 BAR domain is not critical during this step of the CME and IDR is more important. The SH3 domain was
313 unnecessary for CIP4 assembly (Fig. 3a–3c, Extended Data Fig. 4a). However, it is necessary to recruit N-
314 WASP and subsequently form the asymmetric bulge.

315 A CIP4-rich condensate near the CCP is then supposed to recruit other related proteins into the
316 condensate (Fig. 6d). Compared to HR1, GBD of N-WASP has a higher affinity to Cdc42 and will completely
317 displace the HR1 to interact with Cdc42, which further exposes the C-terminal acidic region, allowing the
318 further recruitment and activation of the Arp2/3 complex[52]. We demonstrated that N-WASP also had a high

319 LLPS propensity and co-existed with CIP4 in the same droplet *in vitro* (Figs. 5c, 5h), suggesting that the CIP4
320 condensate recruits and accommodates N-WASP. Consequently, the local concentration of the active Arp2/3
321 complex also increases, which accelerates actin polymerisation (Figs. 6d, 6e). A similar process had been
322 demonstrated using Toca1, a subfamily member of CIP4 with conserved HR1 and SH3 domains[36,52],
323 suggesting a conserved role of CIP4 subfamily proteins in mediating Cdc42-WASP-Arp2/3 actin signalling.
324 Moreover, recent studies revealed that actin-associated proteins with a long IDR, such as vasodilator-
325 stimulated phosphoprotein and actin-binding LIM protein 1, formed liquid droplets under physiological
326 conditions and promoted actin polymerisation and bundling[53,54]. Our *in vitro* assay demonstrated that G-actin
327 preferred to localise in the condensed phase of CIP4-FDR (Fig. 5i), implying that the concentration of free G-
328 actin increases in the CIP4-rich phase near the CCP, which also promotes actin polymerisation.
329 We speculate that 'branched actin', not the CIP4 condensate, generates the mechanical force to
330 deform the plasma membrane. CK666 inhibited actin polymerisation, which consequently inhibited the
331 membrane protrusion (Fig. 1b, Extended Data Fig. 1f), indicating that the major driving force of the
332 protrusion is Arp2/3-mediated actin polymerisation. Electron microscopic observations revealed that branched
333 actin fibres near the CCP are highly anisotropic[17]. However, Arp2/3 produces branched fibres with a fixed
334 angle (~70°). This finding suggests that actin fibres expand in a radial orientation and push the nearby
335 membrane, resulting in membrane bulge (upward) and fusion (lateral) (Fig. 6e). It may also generate a
336 downward force to push the CCP toward the cell interior, as suggested by another group[55]. Further studies are
337 required to elucidate this mechanism.
338 The BAR/F-BAR scaffolds interplay with dynamin during the membrane scission process[56]. One
339 classic example is the opposite role of Sorting nexin 9 (SNX9) and Amphiphysin in regulating the activity of
340 dynamin at the late stage of endocytosis. SNX9 recruits dynamin and promotes the assembly-stimulated
341 GTPase activity of dynamin by stabilising the dynamin-membrane interaction[57,58] (Fig. 6f). By contrast,
342 Amphiphysin is recruited by dynamin and inhibits the dynamin ring formation by destabilising the dynamin-
343 membrane interaction[59,60] (Fig. 6f). Current evidence is not yet sufficient to illustrate the functional interplay
344 between CIP4 or CIP4-mediated actin polymerisation and dynamin. Nevertheless, we have observed that
345 dynamin depletion[27] and actin inhibition did not completely abolish CME progression (Fig. 1b, Extended Data
346 Fig. 1f), suggesting that actin- and dynamin-driven pit-closing may function as relatively independent

347 mechanisms and either could be dominant depending on free actin abundance (Fig. 6f). However, membrane
348 tabulation induced by the F-BAR domain could be antagonised by dynamin- and membrane-associated actin
349 cytoskeleton[61]. Moreover, each dynamin helix can capture 12–16 actin filaments and align them into
350 bundles[62]. Therefore, it is also reasonable to propose that dynamin may further potentiate the CIP4-induced
351 actin cytoskeleton reorganisation, which promotes dynamin-dependent scission processes such as the super
352 twist of the dynamin helix[63]. However, these speculations should be further studied.
353

354 **Methods**

355 ***Plasmids***

356 Mammalian expression vectors encoding pEGFP-N1-CLTB and pmCherry-C1-CLTB were constructed as
357 described previously[27]. Fragments of the full-length (FL) CIP4 (amino acids (a.a.) 1–547), FL-FBP17 (a.a. 1–
358 617), FL-Synd2 (a.a. 1–486), CIP4-F-BAR (a.a. 1–257), CIP4-FDR (a.a. 258–489), CIP4(ΔSH3) (a.a. 1–489),
359 and CIP4(ΔIDR2/SH3) (a.a. 1–425) were amplified using PCR and subcloned into pmCherry-C1 vectors for
360 mammalian expression. Fragments of CIP4-FDR (a.a. 258–489), FBP17-FDR (a.a. 258–552), Synd2-IDR
361 (a.a. 276–428), CIP4-FDR-ΔIDR1 (a.a. 339–489), CIP4-FDR-ΔIDR2 (a.a. 258–425), CIP4-HR1 (a.a. 339–
362 425), CIP4-SH3 (a.a. 490–547), and N-WASP-GBD (a.a. 197–255) were amplified using PCR and subcloned
363 into pET28a (+) or pGEX-6P-1 vectors for expression in *Escherichia coli*.
364 Vectors encoding mCherry-fused and EGFP-fused CSS chimeric molecules were constructed by amplifying
365 and ligating the DNA fragments corresponding to CIP4 (a.a. 1–257) and Synd2 (a.a. 276–486) and subcloning
366 into pEGFP-C1 and pmCherry-C1 vectors. Similarly, the SCC chimaera fragment was obtained by amplifying
367 and ligating the nucleotide sequence corresponding to Synd2 (a.a. 1–275) and CIP4 (a.a. 258–547). The DNA
368 fragments corresponding to CIP4-SH3 (a.a. 490–547) and Synd2-SH3 (a.a. 429–486) were deleted from the
369 SCC or CSS fragments, respectively, using PrimerSTAR® Max DNA Polymerase (Takara Bio Inc., Shiga,
370 Japan) to obtain the fragments of SC and CS chimaera. CIP4-FDR(ΔHR1) fragment was obtained by deleting
371 the nucleotide sequence corresponding to CIP4-HR1 (a.a. 339–425) using PrimerSTAR® Max DNA
372 Polymerase.

373 Single and multiple amino acid mutations were introduced using PrimerSTAR® Max DNA Polymerase. The
374 MGD to IST mutation was generated by replacing the amino acids of M381, G382, and D383 with I, S, and T,
375 respectively; the 4S mutation was generated by replacing the amino acids of L347, L401, Y408, and W411
376 with S; the W524K mutation was generated by replacing the amino acids of W524 with K.
377 Cdc42 (a.a. 1–191) and N-WASP (a.a. 1–509) fragments were amplified using PCR and subcloned into
378 pEGFP-C1 and pET28a (+) vectors for mammalian and bacterial expression, respectively. pcDNA3-EGFP-
379 Cdc42(T17N) and pcDNA3-EGFP-Cdc42(Q61L) were obtained from Klaus Hahn (Department of
380 Pharmacology, University of North Carolina School of Medicine; Addgene; plasmid # 12600 and 12601)[64].
381
382 ***Expression and purification of recombinant proteins***
383 The following recombinant proteins were used herein: hexa-histidine-tagged CIP4-FDR, FBP17-FDR, Synd2-
384 IDR, CIP4-FDR(4S), CIP4-FDR(IST), CIP4-HR1, CIP4-HR1(4S), CIP4-FDR(ΔHR1), CIP4-FDR(ΔIDR1),
385 CIP4-FDR(ΔIDR2), Cdc42, Cdc42(Q61L), and N-WASP and glutathione S-transferase (GST)-tagged CIP4-
386 SH3, CIP4-SH3(W524K), and N-WASP-GBD. Vectors encoding the recombinant proteins were constructed
387 as described in the previous section and introduced into the BL21-CondonPlus (DE3)-RIL competent cells
388 (Agilent Technologies, Inc., Santa Clara, CA, USA) via heat shock at 37 °C for 30 s. The expression of the
389 recombinant protein was induced using 0.5 mM isopropylthio-β-D-galactoside at 16 °C for 16 h. Bacterial
390 cells expressing hexa-histidine-tagged or GST-tagged recombinant proteins were harvested and resuspended
391 with phosphate-buffered saline (PBS; 137 mM NaCl, 2.7 mM KCl, 10 mM Na_2HPO_4, and 1.8 mM KH_2PO_4;
392 pH 7.4) containing lysozyme (0.2 mg/mL), DNaseI (20 μg/mL), $MgCl_2$ (1 mM), and
393 phenylmethanesulfonylfluoride (1 mM). The cells were subjected to freeze–thaw cycles thrice and
394 homogenised via sonication. Insoluble cell debris was removed via centrifugation at 13,000 g, 4 °C for 15
395 min. The cleared lysate was then mixed with nickel-nitrilotriacetic acid (Ni-NTA)-agarose beads (QIAGEN,
396 Hilden, Germany) or glutathione (GSH) Sepharose 4B beads (Cytiva, Marlborough, MA, USA), and
397 incubated at 4 °C for 1 h with rotation to collect tagged proteins. The Hexa-histidine- and GST-tagged
398 proteins were eluted with Elution buffer A (100 mM NaCl, 50 mM HEPES, 0.2 mM DTT, and 400 mM
399 Imidazole; pH 7.4) and Elution buffer B (100 mM NaCl, 50 mM HEPES, 0.2 mM DTT, and 200 mM GSH;

400 pH 7.4), respectively, and dialysed against a buffer containing 200 mM NaCl and 50 mM HEPES (pH 7.4) at
401 4 °C for 6 h. Proteins were concentrated using AmiconUltra (M.W. 3,000 Da; Sigma-Aldrich, St. Louis, MO,
402 USA) and stored at -80 °C before use.
403
404 ***Pull-down assay***
405 The recombinant proteins (~5 μg) were immobilised on ~20 μL of Ni-NTA agarose or GSH Sepharose 4B
406 beads. EGFP-fused Cdc42 and EGFP-fused N-WASP were expressed in HEK293T cells. The cell pellet was
407 resuspended with PBS containing Protease Inhibitor Cocktail (0.5%, Nacalai Tesque, Inc., Kyoto, Japan) and
408 Triton-X-100 (0.25%) on ice for 10 min. The cell lysate containing EGFP-Cdc42 (WT or T17N) was
409 incubated with GTPγ-S or GDP as described previously to activate Cdc42[65]. The cell lysate was mixed with
410 the purified recombinant protein and Ni-NTA or GSH beads and incubated at 4 °C for 25 min, and the bound
411 fraction was eluted with 400 mM imidazole or 100 mM GSH in Elution Buffer (100 mM NaCl, 50 mM
412 HEPES, 0.2 mM DTT; pH 7.4), respectively. Approximately 20% of the bound and 10% of the unbound
413 fraction were analysed using immunoblotting and SDS-PAGE, respectively.
414
415 ***Cell culture and transfection***
416 Monkey kidney-derived fibroblast-like cells (Cos7 cells) purchased from the Cell Engineering Division in
417 RIKEN BioResource Center (RBC0539; Ibaraki, Japan) were cultured in high-glucose Dulbecco's modified
418 Eagle's medium (DMEM) supplemented with 10% foetal bovine serum at 37 °C with 5% CO_2. For HS-AFM
419 observation, slide glasses (Matsunami Glass Ind., Ltd., Osaka, Japan) or 0.15 CG pierced slide glass (ToA
420 Optical Technologies, Inc., Tokyo, Japan) were coated with 0.01% poly-L-lysine solution (Sigma-Aldrich)
421 and incubated at 37 °C for 1 h. Cos7 cells were seeded on the glass, incubated overnight, and subjected to HS-
422 AFM observation the next day. CK666 (Abcam, Cambridge, United Kingdom) was added to the culture
423 medium to a final concentration of 100 μM 30 min before the observation. Polyethyleneimine (M.W. 40,000,
424 Polyscience, Niles, IL, USA) was used to introduce the expression vectors into Cos7 cells.
425
426 ***RNA interference***

427 Cos7 cells were transfected with siRNA using the HiPerfect reagent (QIAGEN) according to the
428 manufacturer's protocol. siRNA against CIP4 (ID: s17814, 5′-GGAGAAUAGUAAGCGUAAATT-3′),
429 FBP17 (ID: s22916, 5′-CAACCUAAAAAGAACUCGATT-3′), or Synd2 (ID: s22216, 5′-
430 AGAUGUUCUUAAGACCAAATT-3′) were purchased from Ambion Inc. (Austin, TX, USA). siRNA
431 targeting the 3′UTR sequence of CIP4 was customised at Thermo Fisher Scientific (Waltham, MA, USA).
432 siRNA against N-WASP (siGENOME SMART pool) was purchased from Dharmacon Inc. (Lafayette, CO,
433 USA). The cells were treated with trypsin 48 h after the transfection and seeded on slide glasses for HS-AFM
434 observation or directly harvested and analysed using SDS-PAGE followed by immunoblotting. The rescue
435 experiment was performed by transfecting Cos7 cells with siRNA against CIP4 48 h before the observation
436 and transfecting the cells with vectors encoding mCherry-tagged SC chimaera 24 h before the observation.
437

438 ***HS-AFM imaging and image analyses***

439 A tip-scan type HS-AFM system (BIXAM^{TM}; Olympus Corporation, Tokyo, Japan) combined with a confocal
440 microscope (FV1200, Olympus Corporation)[27,66,67] was used for AFM imaging. The HS-AFM system uses a
441 tapping mode with a phase feed-back control. An electron beam-deposited ultra-short cantilever (USC-F0.8-
442 K0.1-T12-x66-10; Nonoworld Corporation, Neuchâtel, Switzerland) with a spring constant of 0.1 N m^{-1} was
443 used for scanning. We performed all imaging using a cantilever amplitude of 85–92% of its free amplitude.
444 Images were acquired every 2 s to analyse the detailed morphological characteristics of the undetermined
445 closing pattern. Images were acquired every 10 s owning to the mutual compensation between scanning speed
446 and scanning area to observe clathrin pits generally. When images were acquired every 10 s, the total scanning
447 area was 6000 × 4500 nm^2 and was displayed in 320 pixels × 240 pixels images. All observations were
448 performed at 28 °C. The correlative imaging of HS-AFM and confocal microscopy was performed as
449 described previously[22].

450 Time-lapse HS-AFM images were acquired using AFM Scanning System Software Version 1.6.0.12
451 (Olympus Corporation). The diameter, duration, and height of the membrane bulge were analysed using the
452 Gwyddion software (ver 2.55; http://gwyddion.net/) and GIMP software (ver 2.10.18; https://www.gimp.org/).
453 The highest point of the plasma membrane at the CCP area was recorded and compared with the surrounding
454 plasma membrane to record the height of the membrane bulge. The lowest position in the HS-AFM image was

455 set as ‘0’ automatically. The duration of the membrane bulge was counted from the first image with the visible
456 membrane bulge to its complete disappearance. Regarding the pit’s size, its maximum diameter during the
457 entire CME process was measured by first doing a cross-section and measuring the distance between one side
458 of the pit and the other. Concerning cases with no detectable membrane bulge (undetermined pattern), the
459 height and duration were set as ‘0 μm’ and ‘0 s’, respectively. By plotting the change of membrane height at
460 the pit area and pit diameter against time, the slope of the ascending part of the height-time plot was used to
461 obtain the growth rate of the membrane bulge. By contrast, the slope of the descending part of the diameter-
462 time plot was used to obtain the closing rate of CCPs.
463
464 ***Immunoblotting***
465 The total cell lysate from Cos7 cells expressing EGFP-fused CIP4, FBP17, or Synd2 and from Cos7 cells
466 subjected to single KD of CIP4, FBP17, or Synd2 was separated using 12% SDS-PAGE gel, transferred to a
467 polyvinylidene difluoride membrane, blocked in 5% skimmed milk in tris buffered saline (5 mM Tris, 13.8
468 mM NaCl, 0.27 mM KCl, pH 7.4) containing 0.1% Tween (Nacalai Tesque, Inc.), and incubated with a
469 primary antibody for 1 h. The following antibodies were used: rabbit anti-CIP4 (1:1000; Bethyl Laboratories
470 Inc., Montgomery, TX, USA), rabbit anti-pacsin2 (1:1000; Novus Biologicals LLC, Centennial, CO, USA),
471 rabbit anti-FNBP1 (1:1000; Novus Biologicals LLC), rabbit anti-N-WASP (1:1000; Cell Signaling
472 Technology, Danvers, MA, USA), rabbit anti-GFP (1:1000; Medical & Biological Laboratories Co., Ltd.,
473 Nagano, Japan), and mouse anti-β-actin (1:1000; Sigma-Aldrich). The blot was then incubated with a
474 secondary antibody: goat anti-rabbit IgG (H+L) antibody (1:5000; Thermo Fisher Scientific) or Goat anti-
475 mouse IgG (H+L) antibody (1:5000; Cytiva) at 27 °C for 1 h. The immunoreactive bands were visualised
476 using Chemi-Lumi One Super Kit (Nacalai Tesque) under a LAS-3000 Imager (Fujifilm, Tokyo, Japan).
477
478 ***Live-cell fluorescence microscopy***
479 A confocal laser-scanning microscope (FV3000, Olympus Corporation) equipped with a stage incubator
480 (TOKAI HIT Corporation, Shizuoka, Japan) was used for live-cell imaging. The lateral spatial resolution is
481 ~200 nm under optimised operation. All observations were performed at 37 °C, under 5.0% CO_2. Cos7 cells
482 were seeded on a 30-mm glass-bottom dish with 40% density and transfected with the vectors mentioned

483 earlier 24 h before imaging. Time-lapse fluorescence images were captured every 5 s and analysed with
484 ImageJ (ver 1.52a; https://imagej.nih.gov) and the GIMP software (ver 2.10.18).
485
486 ***Super-resolution SIM live-cell imaging***
487 Super-resolution SIM was performed using Elyra 7 with Lattice SIM^2 (Zeiss, Oberkochen, Germany). The
488 lateral spatial resolution was ~60 nm under optimised operation conditions. Regarding two-colour live-cell
489 imaging, Cos7 cells with 40% cell density were seeded on a 30-mm glass-bottom dish and transfected with
490 vectors encoding EGFP-fused CLTB and mCherry-fused CIP4 24 h before imaging. The culture medium in
491 the dish was exchanged with the phenol red-free DMEM (Sigma-Aldrich) 30 min before imaging. Images
492 were taken every 0.5 s and processed with the Zeiss Enz 3.6 blue edition software. The images were analysed
493 with ImageJ (ver 1.52a).
494
495 ***Circular dichroism (CD) spectroscopy***
496 The CD spectra were acquired with a JASCO J-805 spectropolarimeter (JASCO Corporation, Tokyo, Japan)
497 using 1.0 mL quartz cuvettes with a 5-mm path length. The purified HR1 domain was diluted with 1×PBS to
498 the final concentration of 0.2 mg/mL. The measurements were performed at 25 °C in the 280–198 nm range
499 with a data point interval of 0.2 nm. The obtained spectra were analysed using the Spectra Manager software
500 (ver 1.0, JASCO Corporation), and the reference spectra were provided by Dr. Yang, J.T[68].
501
502 ***Crosslinking assay***
503 BS^3 crosslinkers (Thermo Fisher Scientific) were dissolved in distilled water, added to the protein solution to
504 a final concentration of 2 mM, and incubated at 28 °C for 30 min. Recombinant His-CIP4-HR1 treated with
505 crosslinkers was subjected to SDS-PAGE and silver staining using Silver Stain II Kit (Fujifilm) according to
506 the manufacturer's instruction.
507
508 ***Gel-filtration chromatography***
509 Gel-filtration chromatography was performed with the AKTA purifier system (GE Healthcare, Chicago, IL,
510 USA) controlled by the Unicorn 5.1 software. The running buffer contains 20 mM NaCl, 25 mM HEPES, and

511 0.2 mM 2-mercaptoethanol. Superdex 75 10/300 GL column (Cytiva) with a void volume (Vo) of 7.2 mL was
512 used. The calibration curve was obtained by plotting the molecular weight of marker proteins against the
513 partition coefficient (K_{av}). K_{av} was calculated with the equation: K_{av} = (Ve-Vo) / (Vt-Vo). Ve: elution volume;
514 Vo: void volume; Vt: total volume.
515
516 ***Phase separation assay***
517 Hexa-histidine-tagged recombinant proteins of CIP4-FDR, FBP17-FDR, and Synd2-IDR were used for the
518 phase separation assay. The purified protein (~10 mg/mL) was incubated with ATTO488-maleimide (Thermo
519 Fisher Scientific) at 28 °C for 1 h. The reaction was quenched using 4 mM DTT. Droplet formation was
520 induced by adding 5% polyethene glycol and imaged using fluorescence microscopy (FV3000, Olympus
521 Corporation). For examining interaction with actin, purified actin (Cytoskeleton Inc., Denver, CO, USA) and
522 rhodamine-labelled actin (Cytoskeleton Inc.) were reconstituted with the following buffer: 5 mM Tris-HCl
523 (pH 8.0), 0.2 mM $CaCl_2$, 0.2 mM ATP, and 5% (w/v) sucrose. Rhodamine-labelled and non-labelled actin
524 were mixed at 1:20 to a final concentration of 450 μg/mL and pre-incubated with Mg^{2+} (50 μM) and EGTA
525 (0.2 mM) at 28 °C for 4 min. Purified CIP4-IDR was diluted to 3 mg/mL with the following buffer: 5 mM
526 Tris-HCl (pH 8.0), 1.2 mM ATP, 1.1 mM DTT, 50 mM KCl, 2 mM $MgCl_2$, and 5% (w/v) polyethene glycol
527 (Sigma-Aldrich). Mg^{2+}-charged actin was then added to 45 μg/mL and observed using a fluorescence
528 microscope (FV3000).
529
530 ***Turbidity assay***
531 Recombinant proteins of hexa-histidine-tagged CIP4-FDR, FBP17-FDR, Synd2-IDR, CIP4-FDR-4S, CIP4-
532 HR1, CIP4-HR1(4S), CIP4-FDR(ΔHR1), CIP4-FDR(ΔIDR1) and CIP4-FDR(ΔIDR2) were used in the
533 turbidity assay. Purified proteins were serially diluted with a Dilution Buffer (50 mM HEPES pH 7.4 and 100
534 mM NaCl), mixed with an equal volume of Droplet Buffer (30% polyethene glycol, 50 mM HEPES, 100 mM
535 NaCl, pH 8.0), and incubated at 25 °C for 10 min. The mixture was then transferred to a micro-cuvette
536 (BRANDTech Scientific Inc., ESSEX, CT, USA), and the optical density was measured at 600 nm using a
537 spectrophotometer (JASCO V-630). The saturation concentration (C_{sat}) was obtained by fitting the data with
538 the following equation using OriginPro (v.9.8):

539 $OD_{600} = OD_{max}\ C^n / (C_{sat}^n + C^n)$,

540 where C represents protein concentration.

541

542 ***Multiple sequence alignment***

543 Multiple sequence alignment was performed using the T-Coffee test[54]. Sequence similarity was determined

544 using EMBOSS Needle (https://www.ebi.ac.uk/Tools/psa/emboss_needle/).

545

546 ***Three-dimensional protein structure predictions***

547 The three-dimensional protein structure was predicted using ColabFold (v.1.5.2: AlphaFold2 using MMseqs2)

548 (https://colab.research.google.com/github/sokrypton/ColabFold/blob/main/AlphaFold2.ipynb)[69,70]. The amino

549 acids sequence of CIP4-HR1 used for the prediction is shown in Extended Data Figs. 3d.

550

551 ***Statistical analysis***

552 To analyse the closing patterns of CCPs, relatively equal numbers of CCP images were collected from four

553 different Cos7 cells. The total number of CCPs analysed in each analysis is described in the figure legends.

554 All statistical analyses were performed using the two-tailed Student's *t*-test unless otherwise indicated.

555 Differences were considered significant at $P < 0.05$.

556

557 **Data availability**

558 This study includes no original code deposited in external repositories. Source data are provided with this

559 paper. Any additional information required to reanalyse the data reported in this study is available from the

560 corresponding author upon request.

561

562 **References**

563 1. Anderson, R. G., Brown, M. S. & Goldstein, J. L. Role of the coated endocytic vesicle in the uptake

564 of receptor-bound low density lipoprotein in human fibroblasts. *Cell* **10**, 351–364 (1977).

565 2. Rappoport, J. Z. & Simon, S. M. Real-time analysis of clathrin-mediated endocytosis during cell

566 migration. *J. Cell Sci.* **116**, 847–855 (2003).

567 3. Vieira, A. V., Lamaze, C. & Schmid, S. L. Control of EGF receptor signaling by clathrin-mediated
568 endocytosis. *Science* **274**, 2086–2089 (1996).
569 4. Merrifield, C. J. & Kaksonen, M. Endocytic accessory factors and regulation of clathrin-mediated
570 endocytosis. *Cold Spring Harb. Perspect. Biol.* **6**, a016733 (2014).
571 5. Zaccai, N. R. *et al.* FCHO controls AP2's initiating role in endocytosis through a PtdIns(4,5)P_2-
572 dependent switch. *Sci. Adv.* **8**, eabn2018 (2022).
573 6. Day, K. J. *et al.* Liquid-like protein interactions catalyse assembly of endocytic vesicles. *Nat. Cell*
574 *Biol.* **23**, 366–376 (2021).
575 7. Lehmann, M. *et al.* Nanoscale coupling of endocytic pit growth and stability. *Sci. Adv.* **5**, eaax5775
576 (2019).
577 8. Kadlecova, Z. *et al.* Regulation of clathrin-mediated endocytosis by hierarchical allosteric activation
578 of AP2. *J. Cell Biol.* **216**, 167–179 (2017).
579 9. Henne, W. M. *et al.* FCHo proteins are nucleators of clathrin-mediated endocytosis. *Science* **328**,
580 1281–1284 (2010).
581 10. Yamabhai, M. *et al.* Intersectin, a novel adaptor protein with two Eps15 homology and five Src
582 homology 3 domains. *J. Biol. Chem.* **273**, 31401–31407 (1998).
583 11. Kirchhausen, T. & Harrison, S. C. Protein organization in clathrin trimers. *Cell* **23**, 755–761 (1981).
584 12. Hinshaw, J. E. & Schmid, S. L. Dynamin self-assembles into rings suggesting a mechanism for coated
585 vesicle budding. *Nature* **374**, 190–192 (1995).
586 13. Shnyrova, A. V. *et al.* Geometric catalysis of membrane fission driven by flexible dynamin rings.
587 *Science* **339**, 1433–1436 (2013).
588 14. Galletta, B. J., Mooren, O. L. & Cooper, J. A. Actin dynamics and endocytosis in yeast and mammals.
589 *Curr. Opin. Biotechnol.* **21**, 604–610 (2010).
590 15. Mund, M. *et al.* Systematic nanoscale analysis of endocytosis links efficient vesicle formation to
591 patterned actin nucleation. *Cell* **174**, 884–896.e17 (2018).
592 16. Boulant, S., Kural, C., Zeeh, J. C., Ubelmann, F. & Kirchhausen, T. Actin dynamics counteract
593 membrane tension during clathrin-mediated endocytosis. *Nat. Cell Biol.* **13**, 1124–1131 (2011).

17. Collins, A., Warrington, A., Taylor, K. A. & Svitkina, T. Structural organization of the actin cytoskeleton at sites of clathrin-mediated endocytosis. *Curr. Biol.* **21**, 1167–1175 (2011).

18. Yang, C. *et al.* Actin polymerization promotes invagination of flat clathrin-coated lattices in mammalian cells by pushing at lattice edges. *Nat. Commun.* **13**, 6127 (2022).

19. Tsujita, K. *et al.* Coordination between the actin cytoskeleton and membrane deformation by a novel membrane tubulation domain of PCH proteins is involved in endocytosis. *J. Cell Biol.* **172**, 269–279 (2006).

20. Grassart, A. *et al.* Actin and dynamin2 dynamics and interplay during clathrin-mediated endocytosis. *J. Cell Biol.* **205**, 721–735 (2014).

21. Ferguson, S. M. *et al.* Coordinated actions of actin and BAR proteins upstream of dynamin at endocytic clathrin-coated pits. *Dev. Cell* **17**, 811–822 (2009).

22. Taylor, M. J., Perrais, D. & Merrifield, C. J. A high precision survey of the molecular dynamics of mammalian clathrin-mediated endocytosis. *PLOS Biol.* **9**, e1000604 (2011).

23. Sochacki, K. A., Dickey, A. M., Strub, M. P. & Taraska, J. W. Endocytic proteins are partitioned at the edge of the clathrin lattice in mammalian cells. *Nat. Cell Biol.* **19**, 352–361 (2017).

24. Jin, M. *et al.* Branched actin networks are organized for asymmetric force production during clathrin-mediated endocytosis in mammalian cells. *Nat. Commun.* **13**, 3578 (2022).

25. Shevchuk, A. I. *et al.* An alternative mechanism of clathrin-coated pit closure revealed by ion conductance microscopy. *J. Cell Biol.* **197**, 499–508 (2012).

26. Yu, Y. & Yoshimura, S. H. Investigating the morphological dynamics of the plasma membrane by high-speed atomic force microscopy. *J. Cell Sci.* **134**, jcs243584 (2021).

27. Yoshida, A. *et al.* Morphological changes of plasma membrane and protein assembly during clathrin-mediated endocytosis. *PLOS Biol.* **16**, e2004786 (2018).

28. Kaksonen, M. & Roux, A. Mechanisms of clathrin-mediated endocytosis. *Nat. Rev. Mol. Cell Biol.* **19**, 313–326 (2018).

29. Vasan, R., Rudraraju, S., Akamatsu, M., Garikipati, K. & Rangamani, P. A mechanical model reveals that non-axisymmetric buckling lowers the energy barrier associated with membrane neck constriction. *Soft Matter* **16**, 784–797 (2020).

622 30. Hetrick, B., Han, M. S., Helgeson, L. A. & Nolen, B. J. Small molecules CK-666 and CK-869 inhibit
623 actin-related protein 2/3 complex by blocking an activating conformational change. *Chem. Biol.* **20**,
624 701–712 (2013).
625 31. Rohatgi, R. *et al.* The interaction between N-WASP and the Arp2/3 complex links Cdc42-dependent
626 signals to actin assembly. *Cell* **97**, 221–231 (1999).
627 32. Armstrong, G. & Olson, M. F. Bending over backwards: BAR proteins and the actin cytoskeleton in
628 mammalian receptor-mediated endocytosis. *Eur. J. Cell Biol.* **101**, 151257 (2022).
629 33. Aspenström, P. Roles of F-BAR/PCH proteins in the regulation of membrane dynamics and actin
630 reorganization. *Int. Rev. Cell Mol. Biol.* **272**, 1–31 (2009).
631 34. Fricke, R. *et al.* Drosophila Cip4/Toca-1 integrates membrane trafficking and actin dynamics through
632 WASP and SCAR/WAVE. *Curr. Biol.* **19**, 1429–1437 (2009).
633 35. Prehoda, K. E., Scott, J. A., Mullins, R. D. & Lim, W. A. Integration of multiple signals through
634 cooperative regulation of the N-WASP-Arp2/3 complex. *Science* **290**, 801–806 (2000).
635 36. Ho, H. Y. *et al.* Toca-1 mediates Cdc42-dependent actin nucleation by activating the N-WASP-WIP
636 complex. *Cell* **118**, 203–216 (2004).
637 37. Yamazaki, H., Takagi, M., Kosako, H., Hirano, T. & Yoshimura, S. H. Cell cycle-specific phase
638 separation regulated by protein charge blockiness. *Nat. Cell Biol.* **24**, 625–632 (2022).
639 38. Lin, Y. H., Forman-Kay, J. D. & Chan, H. S. Sequence-specific polyampholyte phase separation in
640 membraneless organelles. *Phys. Rev. Lett.* **117**, 178101 (2016).
641 39. Lyons, H. *et al.* Functional partitioning of transcriptional regulators by patterned charge blocks. *Cell*
642 **186**, 327–345.e28 (2023).
643 40. Zeno, W. F. *et al.* Molecular mechanisms of membrane curvature sensing by a disordered protein. *J.*
644 *Am. Chem. Soc.* **141**, 10361–10371 (2019).
645 41. Zeno, W. F. *et al.* Synergy between intrinsically disordered domains and structured proteins amplifies
646 membrane curvature sensing. *Nat. Commun.* **9**, 4152 (2018).
647 42. Su, M. *et al.* Comparative study of curvature sensing mediated by F-BAR and an intrinsically
648 disordered region of FBP17. *iScience* **23**, 101712 (2020).

649 43. Zeno, W. F., Snead, W. T., Thatte, A. S. & Stachowiak, J. C. Structured and intrinsically disordered
650 domains within Amphiphysin1 work together to sense and drive membrane curvature. *Soft Matter* **15**,
651 8706–8717 (2019).
652 44. Stahelin, R. V. *et al.* Contrasting membrane interaction mechanisms of AP180 N-terminal homology
653 (ANTH) and epsin N-terminal homology (ENTH) domains. *J. Biol. Chem.* **278**, 28993–28999 (2003).
654 45. Miller, S. E. *et al.* CALM regulates clathrin-coated vesicle size and maturation by directly sensing and
655 driving membrane curvature. *Dev. Cell* **33**, 163–175 (2015).
656 46. Qualmann, B., Koch, D. & Kessels, M. M. Let's go bananas: revisiting the endocytic BAR code.
657 *EMBO J.* **30**, 3501–3515 (2011).
658 47. Taylor, K. L. *et al.* Opposing functions of F-BAR proteins in neuronal membrane protrusion, tubule
659 formation, and neurite outgrowth. *Life Sci. Alliance* **2**, e201800288 (2019).
660 48. Shimada, A. *et al.* Curved EFC/F-BAR-domain dimers are joined end to end into a filament for
661 membrane invagination in endocytosis. *Cell* **129**, 761–772 (2007).
662 49. Ditlev, J. A. Membrane-associated phase separation: organization and function emerge from a two-
663 dimensional milieu. *J. Mol. Cell Biol.* **13**, 319–324 (2021).
664 50. Zhao, Y. G. & Zhang, H. Phase separation in membrane biology: the interplay between membrane-
665 bound organelles and membraneless condensates. *Dev. Cell* **55**, 30–44 (2020).
666 51. Frost, A. *et al.* Structural basis of membrane invagination by F-BAR domains. *Cell* **132**, 807–817
667 (2008).
668 52. Watson, J. R. *et al.* Investigation of the interaction between Cdc42 and its effector TOCA1: handover
669 of Cdc42 to the actin regulator N-WASP is facilitated by differential binding affinities. *J. Biol. Chem.*
670 **291**, 13875–13890 (2016).
671 53. Graham, K. *et al.* Liquid-like VASP condensates drive actin polymerization and dynamic bundling.
672 *Nat. Phys.* **19**, 574–585 (2023).
673 54. Yang, S. *et al.* Self-construction of actin networks through phase separation–induced abLIM1
674 condensates. *Proc. Natl Acad. Sci. U. S. A.* **119**, e2122420119 (2022).
675 55. Akamatsu, M. *et al.* Principles of self-organization and load adaptation by the actin cytoskeleton
676 during clathrin-mediated endocytosis. *eLife* **9**, e49840 (2020).

677 56. Daumke, O., Roux, A. & Haucke, V. BAR domain scaffolds in dynamin-mediated membrane fission.
678 *Cell* **156**, 882–892 (2014).
679 57. Soulet, F., Yarar, D., Leonard, M. & Schmid, S. L. SNX9 regulates dynamin assembly and is required
680 for efficient clathrin-mediated endocytosis. *Mol. Biol. Cell* **16**, 2058–2067 (2005).
681 58. Ramachandran, R. & Schmid, S. L. Real-time detection reveals that effectors couple dynamin's GTP-
682 dependent conformational changes to the membrane. *EMBO J.* **27**, 27–37 (2008).
683 59. Meinecke, M. *et al.* Cooperative recruitment of dynamin and BIN/amphiphysin/Rvs (BAR) domain-
684 containing proteins leads to GTP-dependent membrane scission. *J. Biol. Chem.* **288**, 6651–6661
685 (2013).
686 60. Owen, D. J. *et al.* Crystal structure of the amphiphysin-2 SH3 domain and its role in the prevention of
687 dynamin ring formation. *EMBO J.* **17**, 5273–5285 (1998).
688 61. Itoh, T. *et al.* Dynamin and the actin cytoskeleton cooperatively regulate plasma membrane
689 invagination by BAR and F-BAR proteins. *Dev. Cell* **9**, 791–804 (2005).
690 62. Zhang, R. *et al.* Dynamin regulates the dynamics and mechanical strength of the actin cytoskeleton as
691 a multifilament actin-bundling protein. *Nat. Cell Biol.* **22**, 674–688 (2020).
692 63. Cheng, X. *et al.* Dynamin-dependent vesicle twist at the final stage of clathrin-mediated endocytosis.
693 *Nat. Cell Biol.* **23**, 859–869 (2021).
694 64. Nalbant, P., Hodgson, L., Kraynov, V., Toutchkine, A. & Hahn, K. M. Activation of endogenous
695 Cdc42 visualized in living cells. *Science* **305**, 1615–1619 (2004).
696 65. Ma, L., Cantley, L. C., Janmey, P. A. & Kirschner, M. W. Corequirement of specific
697 phosphoinositides and small GTP-binding protein Cdc42 in inducing actin assembly in Xenopus egg
698 extracts. *J. Cell Biol.* **140**, 1125–1136 (1998).
699 66. Zhang, Y. *et al.* In vivo dynamics of the cortical actin network revealed by fast-scanning atomic force
700 microscopy. *Microscopy (Oxf)* **66**, 272–282 (2017).
701 67. Yoshida, A. *et al.* Probing in vivo dynamics of mitochondria and cortical actin networks using high-
702 speed atomic force/fluorescence microscopy. *Genes Cells* **20**, 85–94 (2015).
703 68. Yang, J. T., Wu, C. S. C. & Martinez, H. M. Calculation of protein conformation from circular
704 dichroism. *Methods Enzymol.* **130**, 208–269 (1986).

69. Jumper, J. *et al.* Highly accurate protein structure prediction with AlphaFold. *Nature* **596**, 583–589 (2021).

70. Mirdita, M. *et al.* ColabFold: making protein folding accessible to all. *Nat. Methods* **19**, 679–682 (2022).

Acknowledgements

We thank T. Ozaki, K. Deguchi, S. Dodo, and B. Yi at Kyoto University, Graduate School of Biostudies for their technical assistance. We are especially thankful to Dr. F. Ishidate at the iCeMS Analysis Center, Institute for Integrated Cell-Material Sciences (WPI-iCeMS), Kyoto University Institute for Advanced Study (KUIAS), for his technical assistance in super-resolution structural illumination microscopy (Elyra 7). We also thank Mr. Sakai, Mr. Uekusa, Mr. Yagi, and Mr. Ito for their assistance in constructing and maintaining the HS-AFM system, and Dr. Y. Sasaki at Kyoto University for their useful discussion on protein multimerisation. This work was supported by JSPS KAKENHI Grant Numbers JP18H02436, JP18KK0196, JP19K22422, 19H04830, JP22H05171, and JP23H00369 to S.H.Y. and AMED (Japan Agency for Medical Research and Development) under Grant Number JP18gm5810018 and JP20wm0325009 to S.H.Y.

Author contributions

Experiments were designed by Y.Y. and S.H.Y. Plasmids construction, recombinant protein purification, pull-down assay, cell culture and transfection, live-cell HS-AFM imaging and correlative imaging, live-cell confocal fluorescence microscopy, super-resolution SIM live-cell imaging, and gel-filtration chromatography were performed by Y.Y. Phase separation assay and CD spectroscopy were performed by Y.Y. and S.H.Y. Data analysis was completed by Y.Y. and S.H.Y. Manuscript writing, figure design, and editing was done by Y.Y. and S.H.Y. S.H.Y supervised and funded the project.

Materials and correspondence

Shige H. Yoshimura

Competing interests

The authors declare that they have no conflict of interest.

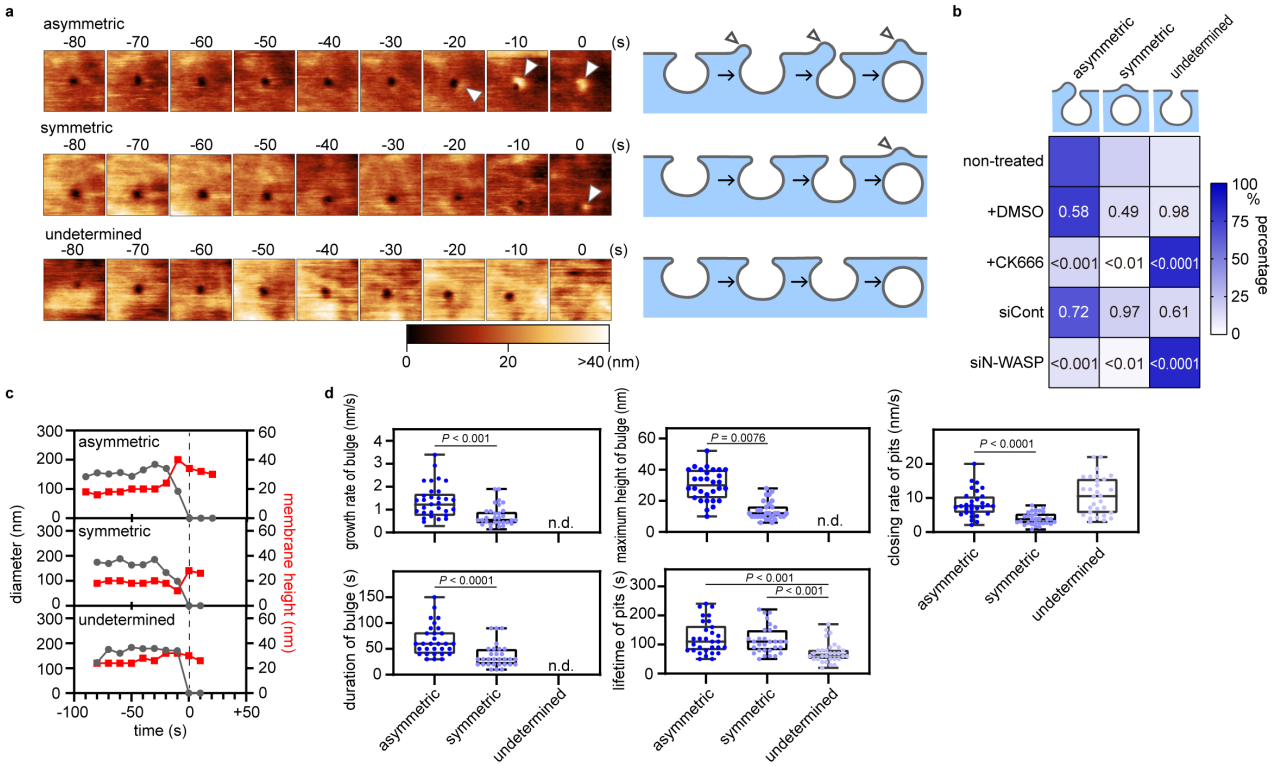

Fig. 1 Asymmetric closing pattern of the CCP.
a, Time-lapse HS-AFM images and schematic illustrations of the asymmetric, symmetric, and undetermined closing patterns of the CCP identified in Cos7 cells. Images were taken every 10 s. Time 0 was when the pit completely closed on the HS-AFM image. Arrowheads indicate the membrane bulge, and the height information of the AFM image is presented using a colour bar. The image size is 1.0 × 1.0 μm^2. Representative images are presented here, and additional images are provided in Extended Data Fig. 1a–1c.
b, Heat map of the ratio of the three CCP closing patterns in non-treated Cos7 cells, Cos7 cells treated with DMSO or CK666, and Cos7 cells transfected with siRNA for the control (luciferase) or N-WASP (N = 4 for each condition). *P* values were calculated by comparing the ratio of the same closing pattern between the non-treated and treated group using a two-tailed Student's *t*-test and indicated in each block, $\alpha = 0.05$.
c, The diameter of CCP (black) and the maximum membrane height at the pit area (red) are plotted against time for the three different closing patterns. A representative case is illustrated in (a). Additional cases are shown in Extended Data Fig. 1a–1c. Time 0 was when the pit completely closed and is indicated with a black dotted line.
d, The growth rate, maximum height, and duration of the bulge, and the total lifetime and the closing rate of CCP in individual closing patterns are plotted (N = 30 for each condition). The median and lower and upper quartiles are indicated in the box. The minimum and maximum values are indicated with the upper and lower whiskers, respectively. In undetermined cases, the height, duration, and growth rate of the membrane bulge were not defined (n.d.). *P* values were calculated using the two-tailed Student's *t*-test, $\alpha = 0.05$.

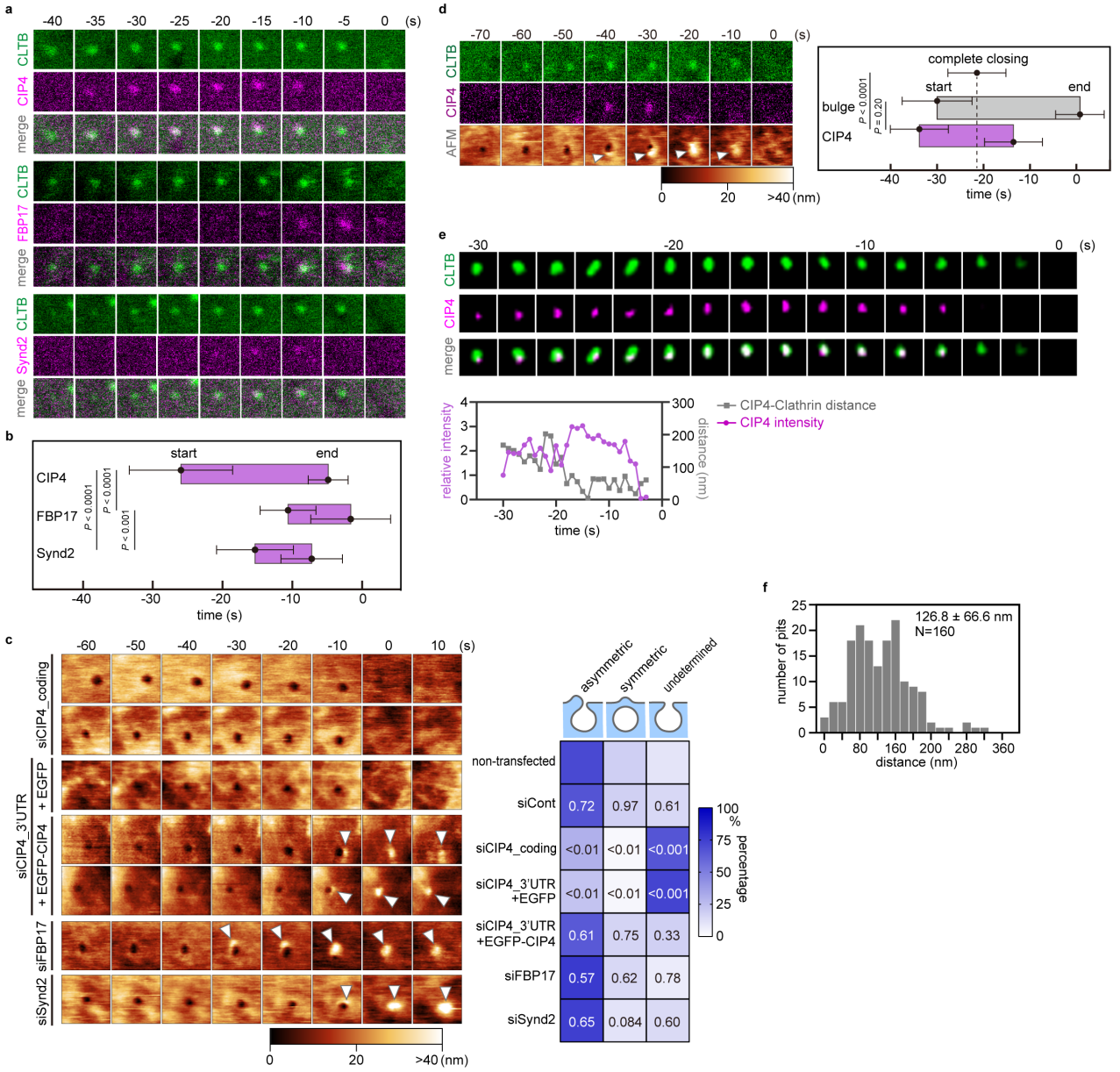

Fig. 2 CIP4 is necessary for asymmetric bulge formation.
a, Time-lapse fluorescence images obtained from Cos7 cells expressing EGFP-fused CLTB and mCherry-fused CIP4, FBP17, or Synd2. Images of 1.0 × 1.0 μm^2 were acquired. Time 0 was when the clathrin signal disappeared. Additional images are provided in Extended Data Fig. 3a–3c.
b, The assembly profile of the F-BAR domain proteins. The times when the fluorescence signal appeared and disappeared at the CCP area are defined as 'start' and 'end', respectively, and are plotted (N = 20 for each condition). Time 0 was when the clathrin signal disappeared. *P* values were calculated using the two-tailed Student's *t*-test, α = 0.05. Error bars represent the standard deviation.
c, (Left) HS-AFM images of Cos7 cells transfected with siRNA for CIP4 (siCIP4_coding, siCIP4_3'UTR), FBP17, or Synd2 followed by EGFP or EGFP-fused CIP4 overexpression. Additional cases are illustrated in ED Fig. 2d. Time 0 was when the pit completely closed on the HS-AFM image. The arrowheads indicate the membrane bulge, and the height information of the AFM image is presented using a colour bar. Image size: 1.0 × 1.0 μm^2. (Right) Heat map of the ratio of three closing patterns in each condition described in the left panel (N = 4, for each condition). *P* values were calculated by comparing the ratio of the same closing pattern between the non-transfected and transfected group using the two-tailed Student's *t*-test and are indicated in each block, α = 0.05.

d, (Left) Correlative imaging of HS-AFM and CLSM. Cos7 cells expressing EGFP-fused CLTB and mCherry-fused CIP4 were imaged. Time 0 was when the pit completely closed on the HS-AFM image. The arrowheads indicate the membrane bulge, and the height information of the AFM image is presented using a colour bar. The image size is 1.0 × 1.0 μm^2. Additional cases are presented in ED Fig. 2g. (Right) The assembly profile of CIP4 and the membrane bulge. The time points when the membrane bulge and the CIP4 signal appeared and disappeared at the CCP area were defined as 'start' and 'end' points, respectively, and are plotted (N=16). *P* values were calculated using the two-tailed Student's *t*-test, $\alpha = 0.05$. Error bars represent the standard deviation.

e, Time-lapse super-resolution images of Cos7 cells expressing EGFP-fused CLTB and mCherry-fused CIP4. Images of 0.5 × 0.5 μm^2 were taken every second and displayed every 2 s. The fluorescence intensity of CIP4 and the x-y distance between the centroids of clathrin and CIP are plotted against time (bottom). Time 0 was when the clathrin signal disappeared. Additional cases are illustrated in ED Fig. 2h.

f, The histogram of the x-y distance between the centroids of the clathrin and CIP4 fluorescence spots within the first 5 s of CIP4 assembly (N = 160, from 32 CMEs).

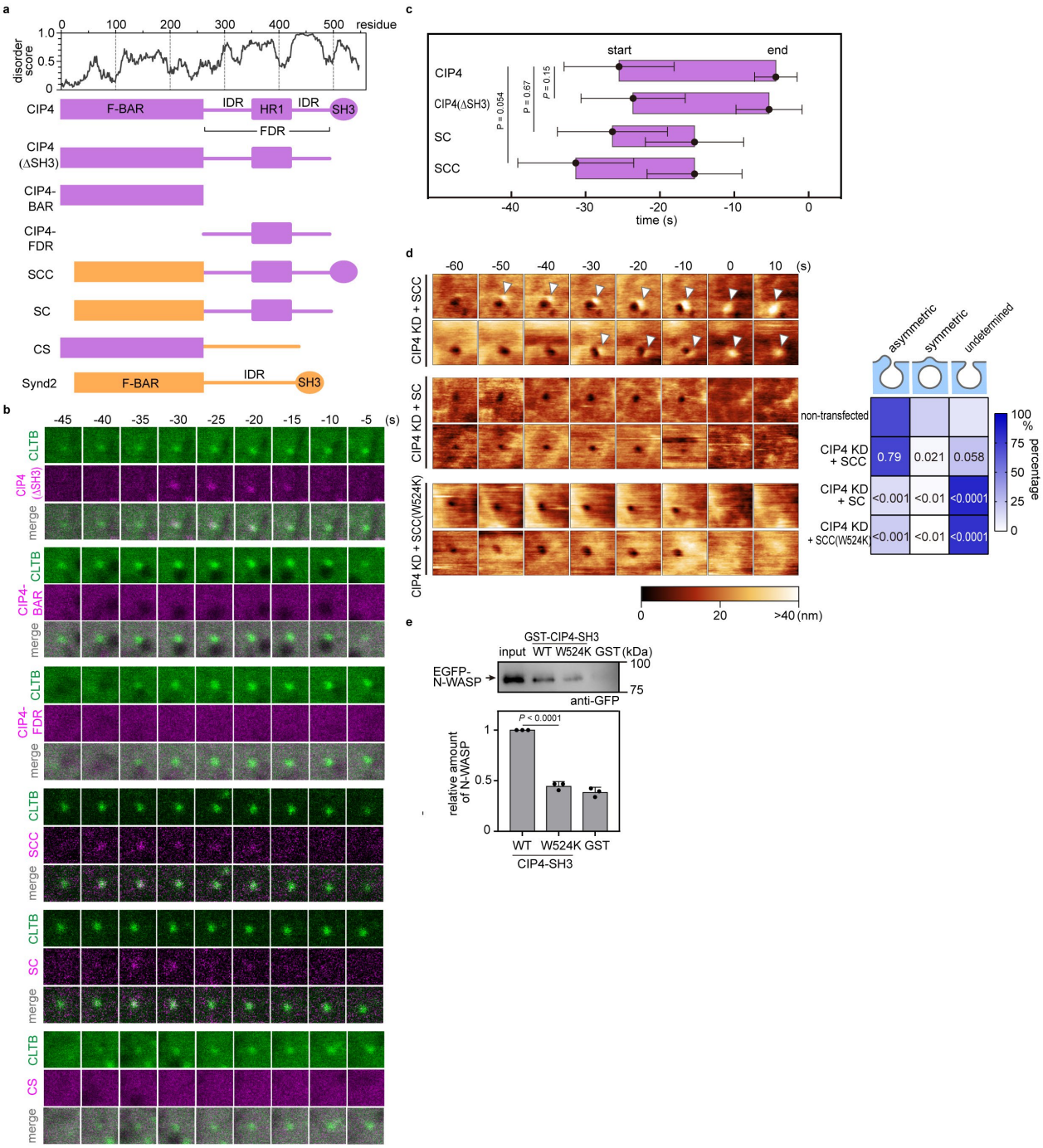

Fig. 3 Flanking disordered region (FDR) and SH3 domain are necessary for asymmetric bulge formation.

a, (Top) Disorder plot of CIP4 predicted using IUPred. (Bottom) Schematic illustration of the domain structures of full-length CIP4 and Synd2, together with their chimeric constructs.

b, Time-lapse fluorescence images obtained from Cos7 cells expressing EGFP-fused CLTB and mCherry-fused CIP4 (WT or chimeric constructs). The image size is 1.0 × 1.0 μm^2. Time 0 was when the clathrin signal disappeared. Representative images are presented here. Additional cases are illustrated in Extended Data Fig. 4a.

c, A summary of the assembly profile of CIP4, CIP4(ΔSH3), and chimeric molecules at CCP. Time 0 was when the clathrin signal disappeared. The timing when the fluorescence signal appeared and disappeared at the CCP area was defined as 'start' and 'end', respectively, and are plotted (N = 20 for each condition). *P*

values were calculated using the two-tailed Student's *t*-test, $\alpha = 0.05$. The error bars represent the standard deviation.

d, Time-lapse HS-AFM images obtained from Cos7 cells expressing EGFP-fused SCC, SC, or SCC(W524K) mutants under the CIP4-KD background. Representative images are presented here. Images were taken every 10 s. Time 0 was when the pit completely closed on the HS-AFM image. The arrowheads indicate the membrane bulge, and the height information of the AFM image is presented using a colour bar. The image size is $1.0 \times 1.0\ \mu m^2$. The frequency of three closing patterns was measured and is summarised in the right panel (N = 4 for each condition).

e, Pull-down assay of CIP4-SH3 and N-WASP. GST-tagged CIP4-SH3(WT) or CIP4-SH3(W524) was mixed with the HeLa cell lysate containing EGFP-fused N-WASP and GSH bead. The eluted fractions were analysed using western blotting with an anti-GFP antibody. The immunoreactive bands were quantified and summarised (bottom). Data are presented as mean ± standard deviation from three independent experiments relative to WT. All data points are shown. *P* values were calculated using the two-tailed Student's *t*-test, $\alpha = 0.05$.

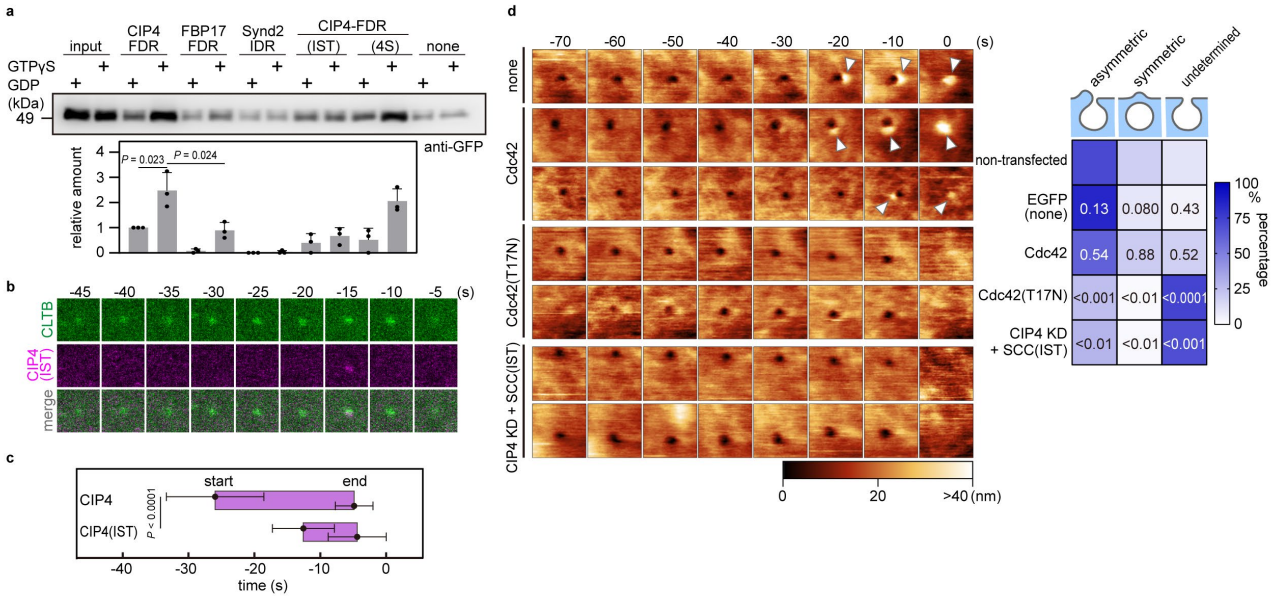

858

859 **Fig. 4 Interaction between Cdc42 and CIP4 is required for the asymmetric bulge.**
860 a, Pull-down assay between Cdc42 and CIP4-FDR, FBP17-FDR, Synd2-IDR, CIP4-FDR(IST), or CIP4-
861 FDR(4S) in the presence of GDP or GTP-γS. Hexa-histidine-tagged recombinant proteins were mixed with
862 the cell lysate containing EGFP-fused Cdc42 in the presence of GDP or GTP-γS. The eluted fraction was
863 subjected to the western blot and is summarised in the bottom panel. Data are presented as mean ± standard
864 deviation from three independent experiments as a relative value to the binding amount between CIP4-FDR
865 and GDP-loaded Cdc42. All data points are shown. *P* values were calculated using the two-tailed Student's *t*-
866 test, α = 0.05.
867 b, Time-lapse fluorescence images of EGFP-fused CLTB and mCherry-fused CIP4 containing MGD to IST
868 mutation expressed in Cos7 cells. The image size is 1.0 × 1.0 μm^2. Time 0 was when the clathrin signal
869 disappeared. Representative images are presented here. Additional cases are presented in Extended Data Fig.
870 5c.
871 c, A summary of CIP4 and CIP4(IST) assembly profiles at CCPs. The timing when the fluorescence signal
872 appeared and disappeared at the CCP area was defined as 'start' and 'end', respectively, and are plotted (N =
873 20, for each condition). *P* values were calculated using the two-tailed Student's *t*-test, α = 0.05. Error bars
874 represent the standard deviation.
875 d, Time-lapse HS-AFM images obtained from Cos7 cells expressing EGFP (none), EGFP-fused Cdc42 (WT
876 or T17N mutant), and the cells expressing EGFP-fused SCC(IST) under the CIP4-KD background.
877 Representative images are presented. Images were taken every 10 s. Time 0 was when the pit completely
878 closed on the HS-AFM image. Arrowheads indicate the membrane bulge, and the height information of the
879 AFM image is presented using a colour bar. The image size is 1.0 × 1.0 μm^2. The frequency of three closing
880 patterns was measured and is summarised in the right panel (N = 4 for each condition).
881

882

883

884

885

886

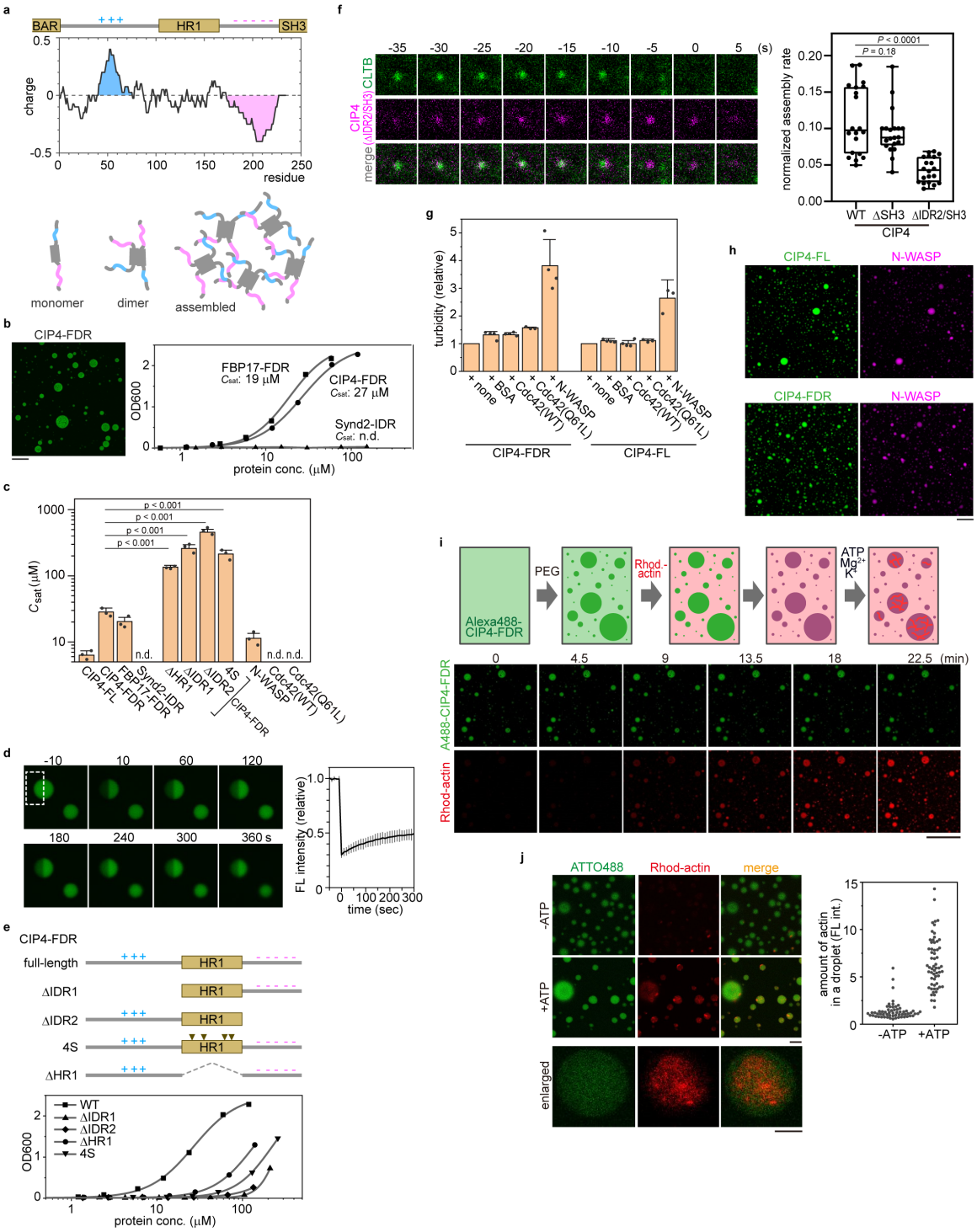

Fig. 5 CIP4-FDR phase separates and promotes actin polymerisation.
a, (Top) A charge plot of CIP4-FDR. HR1 is flanked by net positive (marked in blue) and negative (marked in red) IDRs. (Bottom) A schematic illustration of phase separation of CIP4-FDR driven by charge block interaction.
b, *In vitro* phase separation of FDRs from CIP4 and FBP17 and IDR from Synd2. The turbidity of the solution was measured based on the optical density at 600 nm and plotted against the protein concentration. The saturation concentration (C_{sat}) was obtained via curve fitting (Methods) and is indicated. A representative

895 microscopic image of the CIP4-FDR droplet is also presented. For fluorescence imaging, the protein was pre-
896 labelled with ATTO488. The scale bar is 50 μm.
897 c, The summary of *in vitro* phase separation assay. The C_{sat}. was obtained from the turbidity assay and is
898 summarised. *P* values were calculated using the two-tailed Student's *t*-test, α = 0.05. Error bars represent the
899 standard deviation from more than three independent experiments. All data points are shown. n.d. not
900 determined.
901 D, FRAP analysis of a protein droplet formed by CIP4-FDR. The protein droplet of ATTO488-labelled CIP4-
902 FDR was prepared as indicated in b. Half of the target droplet (dotted square) was bleached via laser radiation,
903 and time-lapse imaging was continued every 10 s. Some representative images are presented. The average
904 fluorescence intensity of the bleached region was quantified and plotted against time as a value relative to that
905 of the pre-bleached signal. Data are presented as mean ± standard deviation from three independent
906 measurements.
907 e, (top) A schematic illustration of CIP4-FDR and its deletion mutants. (bottom) The turbidity assay was
908 performed and plotted as described in (b).
909 f, (Left) Time-lapse fluorescence images of EGFP-fused CLTB and mCherry-fused CIP4(ΔIDR2/SH3)
910 expressed in Cos7 cells. The image size is 1.0 × 1.0 μm^2. Time 0 was when the clathrin signal disappeared.
911 Additional cases are indicated in ED Fig. 6g. (Right) Assembly rate of CIP4 at CCPs was plotted (N = 20 for
912 each condition). The median and lower and upper quartiles are indicated in the box. The minimum and
913 maximum values are indicated with upper and lower whiskers, respectively. *P* values were calculated using
914 the two-tailed Student's *t*-test, α = 0.05.
915 g, The self-assembly of CIP4 is not affected by Cdc42. The relative turbidity of CIP4 (FDR and FL) was
916 measured by the turbidity assays and summarised. Data are presented as mean ± standard deviation from more
917 than three independent experiments. All data points are shown.
918 h, Representative microscopic images of the co-separation of CIP4-FL or CIP4-FDR and N-WASP. For
919 fluorescence imaging, the protein was pre-labelled with ATTO488 or ATTO610. Scale bar, 50 μm.
920 i, (Top) Schematic illustration of actin polymerisation in a protein droplet of CIP4-FDR. After forming a
921 droplet of ATTO488-labelled CIP4-FDR, rhodamine-labelled G-actin was incubated with ATP, Mg^{2+}, and K^+.
922 (Bottom) Time-lapse fluorescence observation of CIP4-FDR (ATTO488-labelled) and G-actin (rhodamine-
923 labelled). Scale bar, 100 μm.
924 j, (Left) A mixture of rhodamine-labelled and non-labelled G-actin (1:9) was loaded with or without ATP and
925 Mg^{2+} and incubated with a pre-formed CIP4-FDR droplet. Representative fluorescence images are presented
926 here. Enlarged images in the presence of ATP are shown below. (Right) Fluorescence intensity of F-actin in
927 the droplet was quantified and is plotted (N = 60 in each condition).
928
929
930
931
932
933
934
935
936
937
938

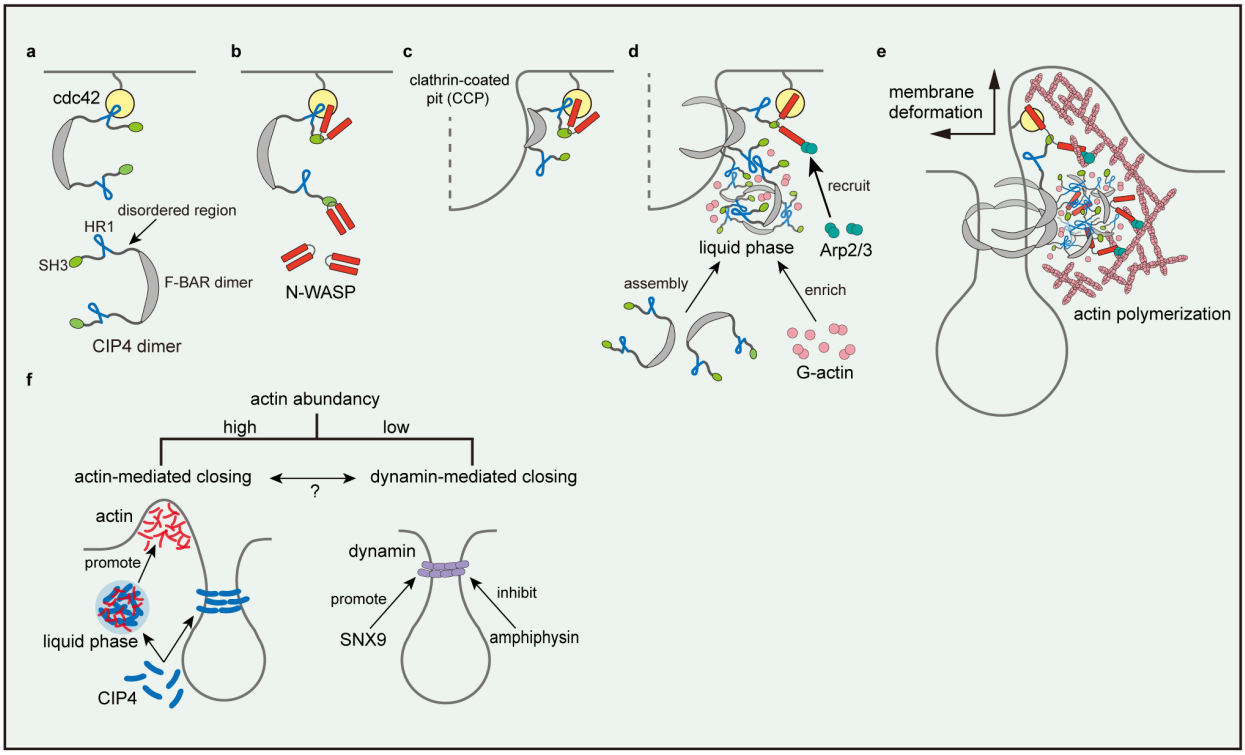

Fig. 6 CIP4 drives the asymmetric CCP closing.
a–e, Schematic illustrations of the CIP4-induced asymmetric CCP closing. Membrane-bound and activated Cdc42 recruits CIP4 via direct interaction with HR1 (a). CIP4 recruits and activates N-WASP to form a ternary complex (b). When the membrane-bound complex approaches a CCP, the F-BAR domain of CIP4 recognises and assembles on the curved membrane (c). This increases the chance of interaction between FDRs and initiates phase separation, resulting in an asymmetric assembly nearby the CCP (d). Meanwhile, activated N-WASP further recruits and activates the Arp2/3 complex, initiating actin polymerisation (d). The condensed phase of CIP4-FDR concentrates G-actin and accelerates the local actin polymerisation, which creates an actin-rich environment (d, e). Activated N-WASP may co-separate with CIP4 in the condensed phase, accelerating Arp2/3 recruitment. Consequently, polymerised actin accumulated rapidly and asymmetrically around CCP which deforms the plasma membrane and promotes the complete closing of the CCP (e).
f, Schematic illustration of the potential correlation between actin- and dynamin-driven pit-closing.

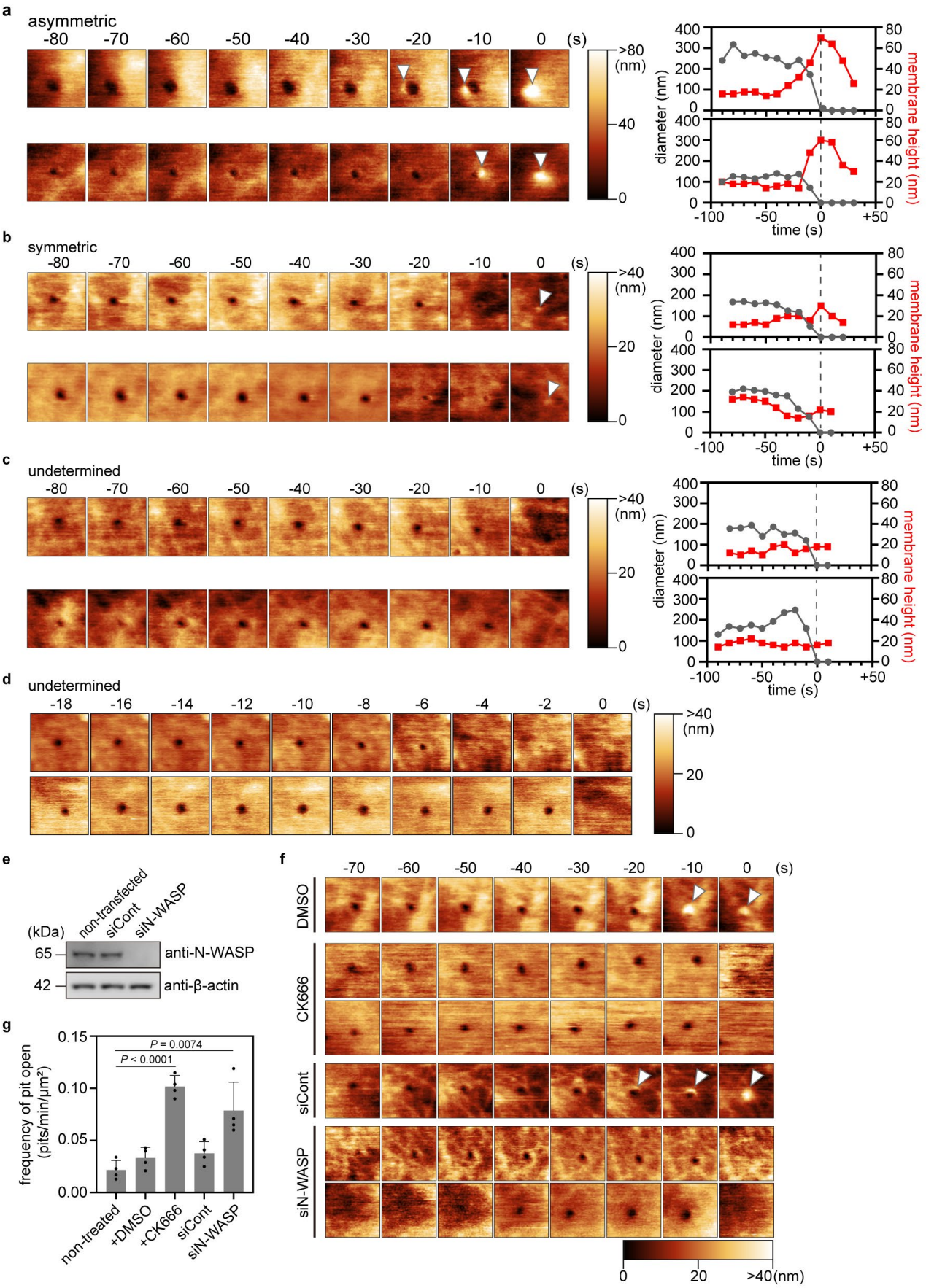
a
asymmetric
-80 -70 -60 -50 -40 -30 -20 -10 0 (s)
>80 (nm)
40
0
diameter (nm)
membrane height (nm)
time (s)
b
symmetric
>40 (nm)
c
undetermined
d
undetermined
-18 -16 -14 -12 -10 -8 -6 -4 -2 0 (s)
e
non-transfected
siCont
siN-WASP
(kDa)
65
42
anti-N-WASP
anti-β-actin
f
DMSO
CK666
siCont
siN-WASP
g
frequency of pit open (pits/min/μm²)
P = 0.0074
P < 0.0001
non-treated
+DMSO
+CK666
siCont
siN-WASP

961

Extended Data Fig. 1 Asymmetric closing pattern of the CCP.

a–c, Additional examples of the time-lapse HS-AFM images of asymmetric (a), symmetric (b), and undetermined (c) closing patterns obtained from Cos7 cells. Details of the experimental conditions and data presentations are the same as those in Figs. 1a, 1c.

d, Time-lapse HA-AFM images of CCPs with the undetermined closing pattern at a scanning rate of 2 s/frame. Time 0 was when the pit completely closed on the HS-AFM image. The height information of the AFM image is presented using a colour bar. The image size was $1.0 \times 1.0\ \mu m^2$.

e, Knockdown efficiency of N-WASP. The total cell lysate of non-transfected Cos7 cells and Cos7 cells transfected with siRNA for the control (luciferase) or N-WASP was prepared 48 h after the transfection and then subjected to the western blot analysis using an anti-N-WASP antibody. β-actin was used as an internal control.

f, Time-lapse HS-AFM images obtained from Cos7 cells treated with DMSO or CK666 and cells transfected with siRNA for the control (luciferase) or N-WASP. Images were taken every 10 s. Time 0 was when the pit completely closed on the HS-AFM image. Arrowheads indicate the membrane bulge, and the height information of the AFM image is presented using a colour bar. Image size: $1.0 \times 1.0\ \mu m^2$.

g, The frequency of CCP formation in non-treated Cos7 cells, the cells treated with DMSO or CK666, and the cells transfected with siRNA for the control (luciferase) or N-WASP were quantified and summarised. Data are presented as mean ± standard deviation from four independent experiments. All data points are shown. *P* values were calculated using the two-tailed Student's *t*-test, $\alpha = 0.05$.

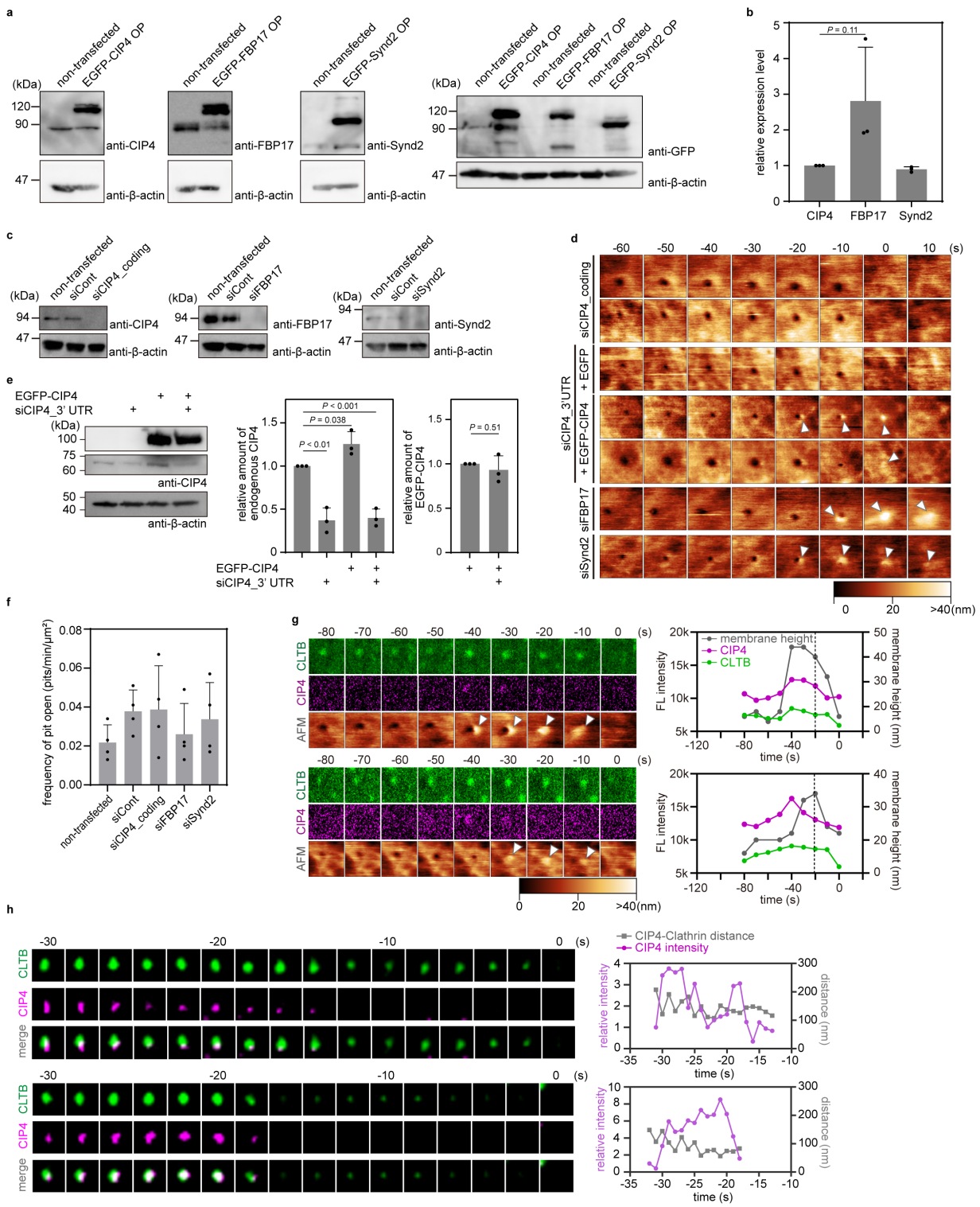

Extended Data Fig. 2 CIP4 is necessary for the asymmetric bulge.
a, The endogenous amount of CIP4, FBP17, and Synd2 in Cos7 cells. The total cell lysate of Cos7 cells expressing EGFP-fused CIP4, FBP17, or Synd2 was subjected to western blotting using anti-CIP4, -FBP17, or -Synd2 antibodies, respectively. The same lysate was also blotted with an anti-GFP antibody for reference. The amount of β-actin was detected with an anti-β-actin antibody as an internal control.
b, The endogenous amount of CIP4, FBP17, and Synd2 obtained from western blotting is indicated in (a). Data from the three independent experiments are summarised. *P* values were calculated using the two-tailed

Student's *t*-test, α = 0.05. Data are presented as mean ± standard deviation from three independent experiments as a relative value to that of CIP4. All data points are shown.

c, Knockdown efficiency of CIP4, FBP17, and Synd2 in Cos7 cells. Total cell lysate of non-transfected Cos7 cells and Cos7 cells transfected with siRNA for the control (luciferase), CIP4, FBP17, or Synd2 was prepared 48 h after the transfection and then subjected to the western blot analysis using anti-CIP4, FBP17, or Synd2 antibodies. β-actin was detected as an internal control.

d, Additional examples of the time-lapse HS-AFM images obtained from Cos7 cells transfected with siRNA against CIP4 (siCIP4_coding), Synd2, or FBP17 and Cos7 cells transfected with siRNA targeting the 3′UTR sequence of CIP4 (siCIP4_3′UTR), followed by the overexpression of EGFP or EGFP-fused CIP4. Details of the experimental conditions and data presentations are the same as those in Fig. 2c.

e. Knockdown efficiency of CIP4 using siRNA targeting the 3′UTR sequence of CIP4 (siCIP4_3′UTR). Total cell lysate of non-transfected Cos7 cells, cells transfected with siCIP4_3′UTR, cells transfected with siCIP4_3′UTR followed by the transfection of plasmids encoding EGFP or EGFP-fused CIP4 was prepared 48 h after the transfection and then subjected to the western blot analysis using anti-CIP4 antibodies. β-actin was used as an internal control. The relative amount of endogenous CIP4 and overexpressed EGFP-CIP4 is summarised in the right panels. Data from the three independent experiments are summarised and presented as mean ± standard deviation. All data points are shown. *P* values were calculated using the two-tailed Student's *t*-test, α = 0.05.

f, The frequency of CCP formation in non-transfected Cos7 cells and Cos7 cells transfected with siRNA for the control (luciferase), CIP4, FBP17, or Synd2 was quantified and is summarised. *P* values were calculated using the two-tailed Student's *t*-test, α = 0.05. No significant differences existed between any two groups. Data are presented as mean ± standard deviation from four independent experiments. All data points are shown.

g, Additional examples of the correlative imaging of HS-AFM and confocal laser-scanning microscopy (CLSM). The fluorescent (FL) intensity of EGFP-fused CLTB and mCherry-fused CIP4 and the maximum membrane height at the CCP area were plotted against time. Time 0 was when the pit completely closed and is indicated with a black dotted line. Other details of the experimental conditions and data presentations are the same as those in Fig. 2d.

h, Additional examples of the time-lapse super-resolution SIM images obtained from Cos7 cells expressing EGFP-fused CLTB and mCherry-fused CIP4. Details of the experimental conditions and data presentations are the same as those in Fig. 2e.

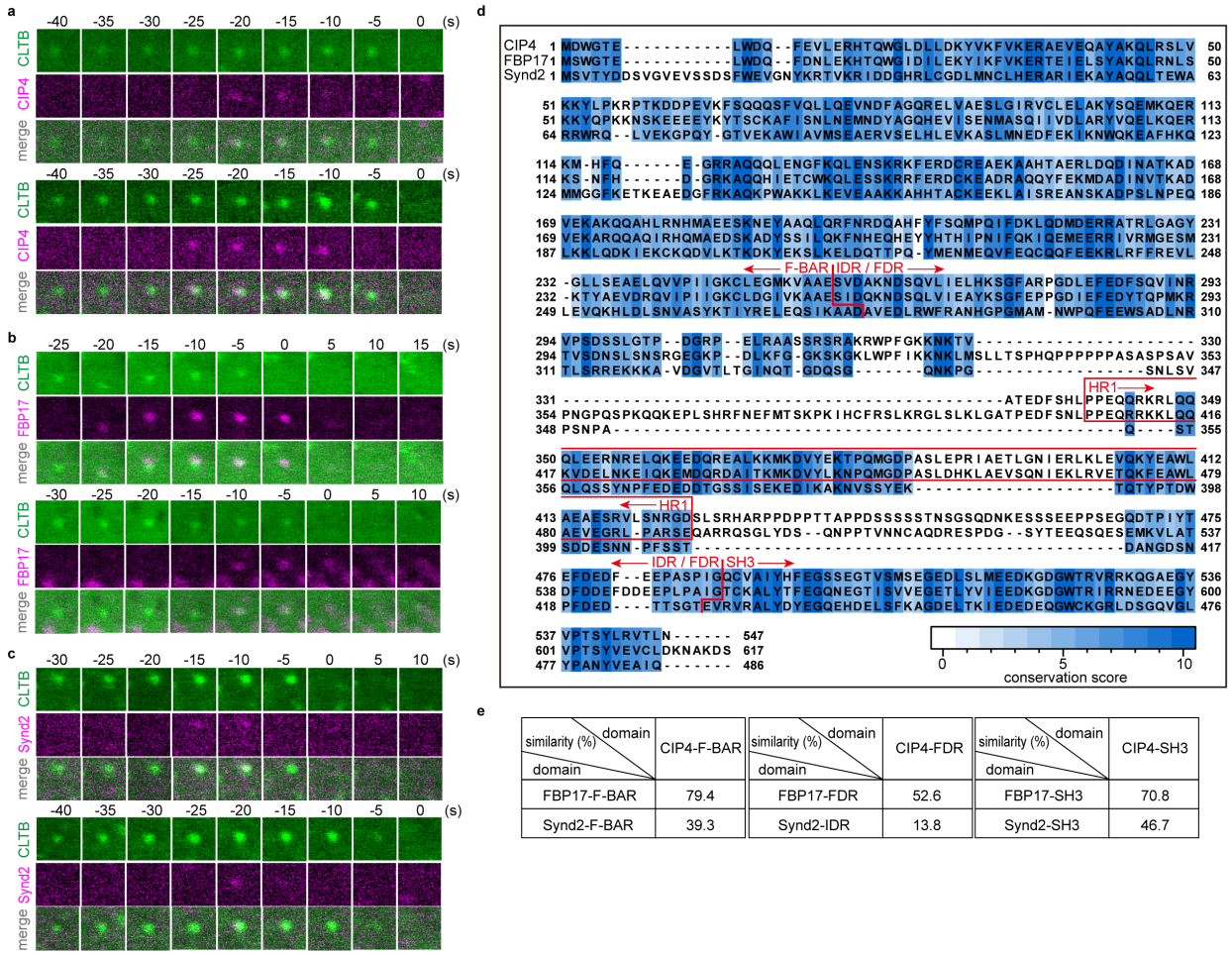

similarity (%) domain / domain	CIP4-F-BAR	similarity (%) domain / domain	CIP4-FDR	similarity (%) domain / domain	CIP4-SH3
FBP17-F-BAR	79.4	FBP17-FDR	52.6	FBP17-SH3	70.8
Synd2-F-BAR	39.3	Synd2-IDR	13.8	Synd2-SH3	46.7

Extended Data Fig. 3 Assembly of F-BAR proteins CIP4, FBP17, and Synd2 to CCP.
a–c, Additional examples of the time-lapse fluorescence images obtained from Cos7 cells expressing EGFP-fused CLTB and mCherry-fused CIP4 (a), FBP17 (b), or Synd2 (c). Details of the experimental conditions and data presentations are the same as those in Fig. 2a.
d, Amino acid sequence alignment of *Mus musculus* CIP4 (Uniprot, Q8CJ53-3), *Homo sapiens* FBP17 (Uniprot, Q96RU3), and *Mus musculus* Synd2 (Uniprot, Q9WVE8). Alignment was performed using T-Coffee. The conservation was scored and presented as indicated in a colour bar. The F-BAR, FDR/IDR, HR1, and SH3 domains are indicated.
e, Pairwise-domain similarity among CIP4, FBP17, and Synd2. The analysis was performed using the EMBOSS Needle.

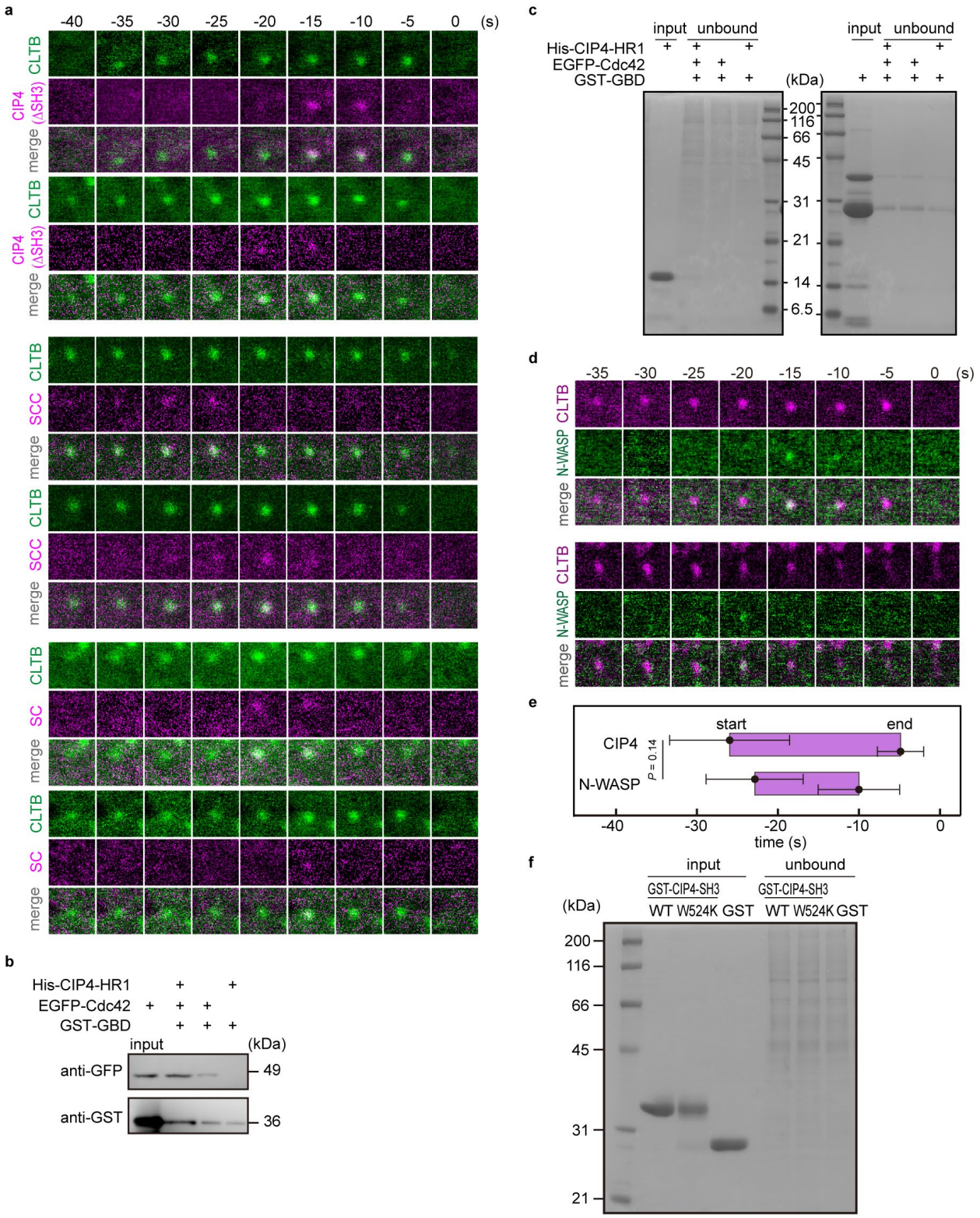

Extended Data Fig. 4 FDR and SH3 domain are necessary for asymmetric bulge formation. a, Additional examples of the time-lapse fluorescence images obtained from Cos7 cells expressing EGFP-fused CLTB and mCherry-fused chimeric CIP4 molecules. Details of the experimental conditions and data presentations are the same as those in Fig. 3b.

b, c, Pull-down assay among CIP4-HR1, Cdc42, and the GBD of N-WASP. GST-tagged GBD was incubated with or without hexahistidine-tagged CIP4-HR1 domain and the cell lysate containing EGFP-fused Cdc42. The eluted fractions were subjected to western blot analysis using an anti-GFP antibody (b). The input amount of CIP4-HR1 and the unbound fraction were analysed using SDS-PAGE (c).
d, Time-lapse fluorescence images of EGFP-fused N-WASP and mCherry-fused CLTB expressed in Cos7 cells. Time 0 was when the clathrin signal disappeared. The image size is $1.0 \times 1.0\ \mu m^2$.
e, A summary of the assembly profile of CIP4 and N-WASP at CCPs. Time 0 was when the clathrin signal disappeared. The timing when the fluorescence signal appeared and disappeared at the CCP area was defined as 'start' and 'end', respectively, and are plotted as mean ± standard deviation (N = 20, for each condition). *P* values were calculated using the two-tailed Student's t-test, $\alpha = 0.05$.
f, Input amount of GST-tagged CIP4-SH3(WT), CIP4-SH3(W524K), empty GST, and the pull-down assay's unbound fraction in Fig. 3e was analysed using SDS-PAGE.

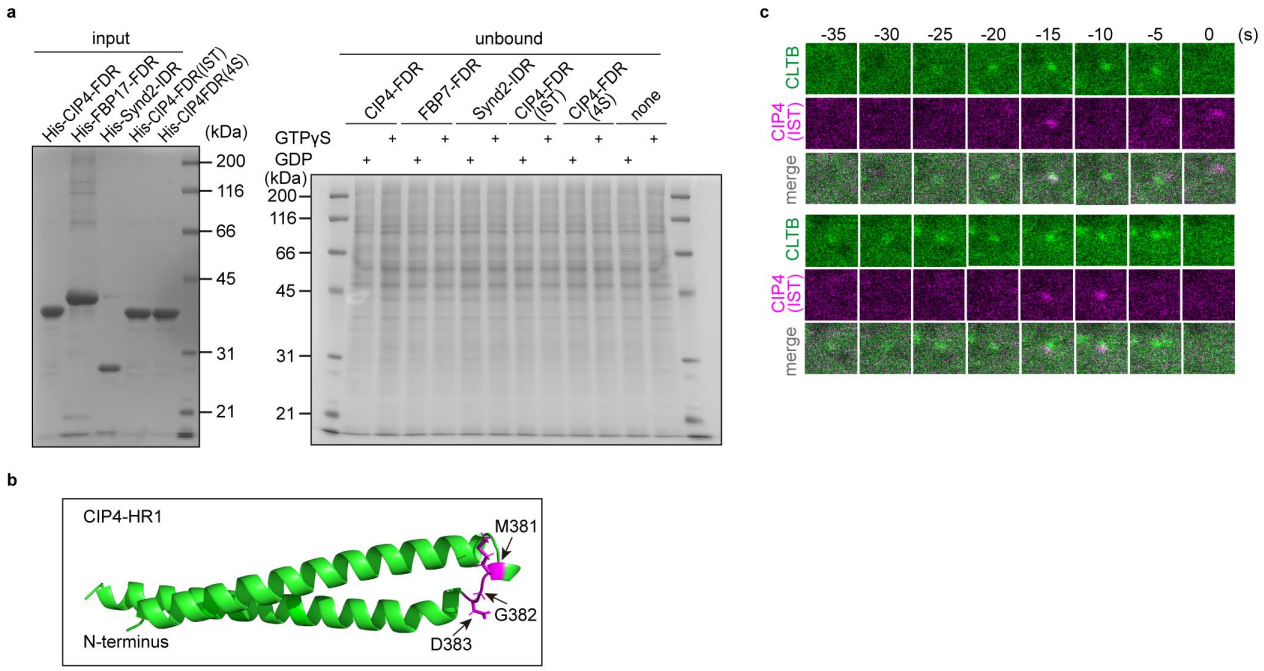

Extended Data Fig. 5 Cdc42 recruits CIP4 to the CCP site.
a, SDS-PAGE analysis of the input and the unbound fraction of the pull-down assay presented in Fig. 4a.
b, A three-dimensional structure of CIP4-HR1 predicted using AlphaFold2. Three mutated residues in CIP4(IST) (M381, G382, D383) are indicated in magenta.
c, Additional examples of the time-lapse fluorescence images of EGFP-fused CLTB and mCherry-fused CIP4(IST) expressed in Cos7 cells. Details of the experimental conditions and data presentations are the same as those in Fig. 4b.

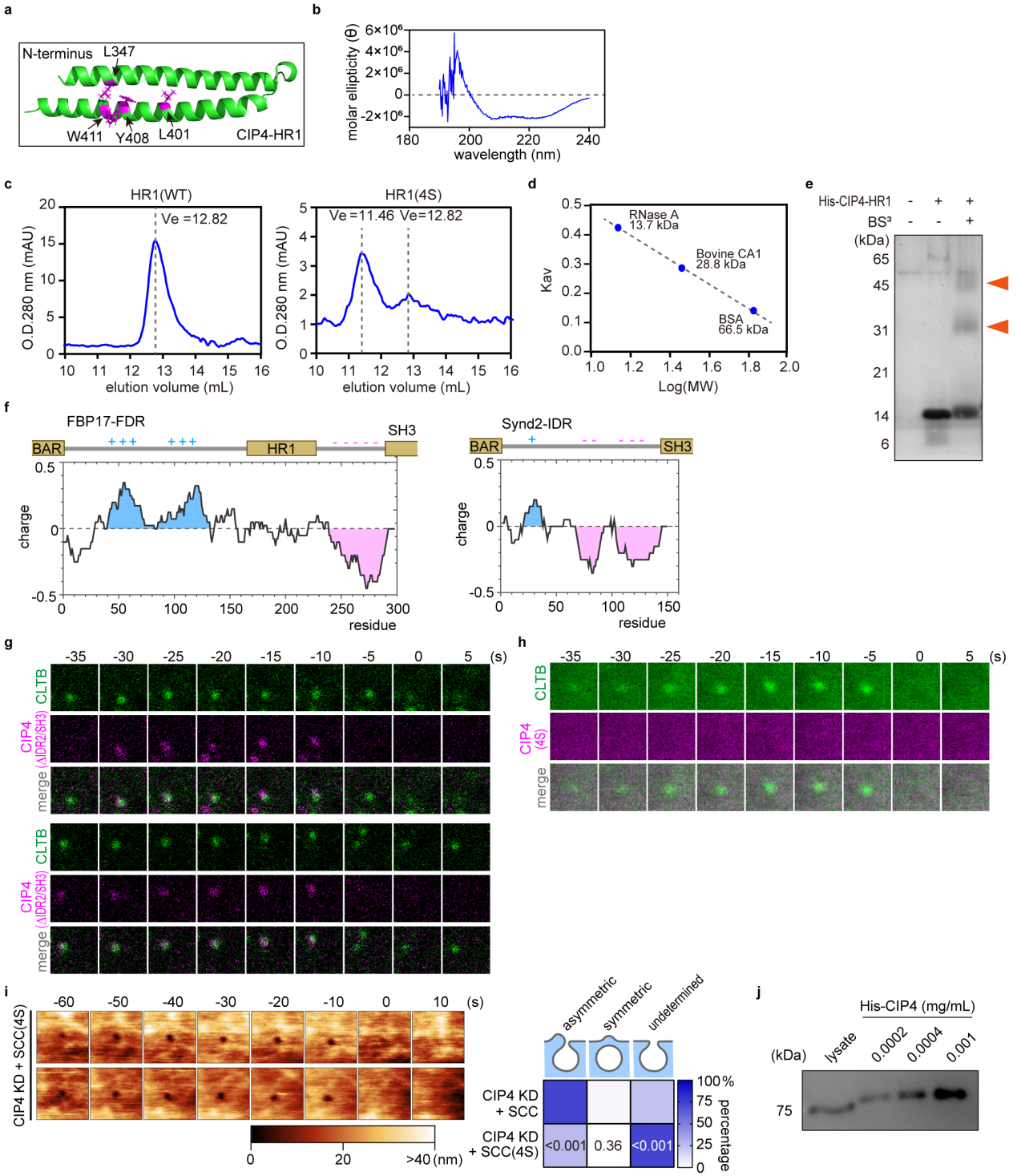

Extended Data Fig. 6 Structural and functional properties of FDRs.
a, Three-dimensional structure of the CIP4-HR1 domain predicted using AlphaFold2. The mutated residues in the CIP4-HR1(4S) are indicated in magenta.
b, Circular dichroism spectrum of purified CIP4-HR1.
c, Gel-filtration chromatography of CIP4-HR1(WT), and CIP4-HR1(4S). The absorbance at 280 nm (mAU) is plotted against the elution volume (mL). The peak position (Ve) is indicated with a dotted line.
d, A size calibration of gel-filtration chromatography shown in b. RNase A (13.7 kDa), bovine carbonic anhydrase 1 (bovine CA-1, 28.8 kDa), and bovine serum albumin (BSA, 66.5 kDa) were analysed. The partition coefficient (K_{av}) obtained from the chromatogram is plotted against the molecular weight.

1138 e, Crosslinking assay of CIP4-HR1. Non-treated and bis(sulfosuccinimidyl)suberate (BS^3)-treated CIP4-
1139 HR1(WT) were subjected to SDS-PAGE, followed by silver staining. Bands of speculated HR1 multimer are
1140 indicated with arrowheads.
1141 f, Charge plot of Synd2-IDR and FBP17-FDR. Positively and negatively charged regions are marked in blue
1142 and red, respectively.
1143 g, Additional examples of the time-lapse fluorescence images of EGFP-fused CLTB and mCherry-fused CIP4
1144 (ΔIDR2/SH3) expressed in Cos7 cells. Details of the experimental conditions and data presentations are the
1145 same as those in Fig. 5f.
1146 h, Time-lapse fluorescence images of EGFP-fused CLTB and mCherry-fused CIP4(4S) expressed in Cos7
1147 cells. The image size was 1.0 ×1.0 μm^2. The time point of the disappearance of the clathrin signal was defined
1148 as '0 s'.
1149 i, Time-lapse HS-AFM images obtained from Cos7 cells expressing EGFP-fused SCC(4S) under the CIP4-
1150 KD background. Images were taken every 10 s. Time 0 was when the pit completely closed on the HS-AFM
1151 image. The height information of the AFM image is presented using a colour bar. The image size was 1.0 ×
1152 1.0 μm^2. The frequency of three different closing patterns was measured and summarised in the right panel (N
1153 = 4 for each condition).
1154 j, Endogenous amount of CIP4 in Cos7 cells. The amount of CIP4 in the total cell lysate of Cos7 cells was
1155 detected using western blotting and compared with *in vitro* purified Hexa-histidine-tagged CIP4 with known
1156 concentration.
1157